



An experimental methodology to characterize load-based fracture models of third generation advanced high strength steel resistance spot welds

Mohammad Shojaee¹ · Cameron Tolton¹ · Abdelbaset Midawi¹ · Tingting Zhang² · Hassan Ghassemi-Armaki³ · Michael Worswick¹ · Cliff Butcher¹ · Elliot Biro¹

Received: 6 December 2023 / Accepted: 11 March 2024 / Published online: 19 March 2024
© The Author(s), under exclusive licence to Springer-Verlag London Ltd., part of Springer Nature 2024

Abstract

Failure of resistance spot welds in computer-aided engineering models is based upon criteria that incorporate test data obtained in various loading conditions including different proportions of tensile, shear, and moment loads. The decomposition of the critical load into its respective shear, tensile, and bending moment components is influenced by the rigid body motion during their corresponding mechanical tests. Continuous tracking of the weld orientation and the deformed coupons is required for accurate determination of the load components at the onset of failure. A comprehensive experimental investigation was performed to characterize the critical failure load components in combined loading using various orientations of KS-II tests and a range of coach peel coupon geometries. Mechanical testing was coupled with digital image correlation (DIC) to systematically evaluate empirical force-based failure models for resistance spot welds of two third generation advanced high strength steels with optimal and suboptimal fusion zone diameters. New analysis methodologies using DIC were developed to account for rotation and deformation of the joint in the determination of the shear, normal, and bending moments acting on the spot-welded joints. The coach peel test results for both steels revealed a non-convex experimental fracture locus in bending-tension loading cases. The conventional assumption of a convex failure locus overestimated the critical bending moment strength between 7 and 66%. Results indicated that changes in the operative failure mechanism from pullout/partial-pullout to interfacial can expand the fracture loci within the shear-tensile loading mixities. Improved alternative functional forms for the weld failure models were proposed and contrasted with conventional models that assume convexity.

Keywords Third-generation advanced high strength steel (3G-AHSS) · Resistance spot welding (RSW) · Mechanical properties · Failure behavior · Coach peel test · Bending moment

1 Introduction

Enhanced fuel efficiency and improved passenger safety are among the most important performance criteria imposed on the automotive industry [1]. Meeting these criteria necessitates manufacturing light automotive structures that exhibit high energy absorption capacity in crash events [2] using high-performance materials such as advanced high-strength steels (AHSS) [3]. Auto manufacturers have incorporated AHSS within their designs with a reported four-fold increase in AHSS adoption from 2006 to 2016 [4, 5]. The recently developed third generation AHSS (3G-AHSS) have the potential for additional weight reduction due to their superior tensile strength-to-ductility ratio compared to the first generation of AHSS (1G-AHSS). Additionally, the use of

✉ Mohammad Shojaee
mshojaee@uwaterloo.ca

¹ Centre for Advanced Materials Joining, Department of Mechanical and Mechatronics Engineering, University of Waterloo, 200 University Avenue West, Waterloo, ON N2L 3G1, Canada

² Advanced Materials Technology - Metallics & Joining, General Motors, Warren, MI 48092, USA

³ General Motors R&D, Materials & Manufacturing Systems Research Laboratory, Warren, MI 48092, USA

3G-AHSS may be a more financially viable option compared to the second generation of AHSS (2G-AHSS) due to reduced alloy content [6]. Joining 3G-AHSS components within vehicle body-in-white (BIW) assemblies is a primary challenge to their industrial application. Resistance spot welding (RSW) is among the most commonly adopted joining techniques within the automotive industry due to its rapid process speed, suitability for automation, and absence of a requirement for filler metals [7]. The RSW joints in a typical modern vehicle play a critical role in maintaining the integrity of the vehicle structure in the case of a crash event. Consequently, the ability to predict the failure of spot welds plays an important role in vehicle design [8].

The available literature regarding spot weld failure prediction can be categorized into two groups: first are the studies that develop a detailed finite element model of the spot-welded joint and assign constitutive properties to different RSW subregions in an attempt to capture information regarding the onset of failure, failure path, and damage evolution [9, 10]. The second group comprises studies that calibrate failure criteria by establishing a relationship between RSW failure loads/stresses and different loading conditions [11–13].

Calibrating a comprehensive weld model that accurately predicts the mechanical performance and failure behavior of a spot-welded joint is challenging due to inhomogeneities in local microstructures and mechanical properties caused by thermal gradients during the RSW process [7]. The property variations in the RSW subregions require local characterization due to the relatively small size of each zone which are typically smaller than 1 mm in length in the heat-affected zones [14]. The so-called hardness scaling approach has been used to predict the mechanical properties of RSW sub-regions. In this approach, the constitutive and fracture behavior of the base material (BM) is scaled depending on the relative hardness ratio between the BM and heat-affected zone (HAZ) or fusion zone (FZ). This technique is reported to give acceptable accuracy in failure prediction of ultra-high-strength press-hardened steel (PHS) resistance spot welds [5, 15, 16]. Recently, Midawi et al. [17] raised concerns regarding the validity of characterizing 3G-AHSS RSW FZs or HAZs using the hardness scaling approach. Compared to PHS steels where the weld zones are comprised of fully martensitic structures of various strengths, the microstructure in the 3G-AHSS RSW sub-regions can be complex and vary significantly from that of the BM [18]. It is questionable to assume that the BM behavior linearly scales with the corresponding hardness ratios. Extraction of miniature coupons directly from the FZ or HAZ [10, 14] or reproduction of representative microstructures using thermomechanical simulators [19, 20] have been used in the literature for local RSW mechanical property evaluation. Ghassemi-Armaki et al. [21] performed extensive

failure characterization under different stress triaxialities for calibration of the BM failure locus which was linearly interpolated to predict HAZ fracture loci. Detailed mesoscopic finite-element models of spot welds have also been considered [9]. Mesoscale models are informative in terms of providing insight into the fracture initiation sites, damage accumulation trends, and crack propagation mechanisms but require extensive BM, HAZ, and FZ fracture characterization. At present, the application of mesoscale models in full BIW assemblies, which contain an average of 6000 spot welds [22], is computationally prohibitive due to the fine mesh size required.

The second approach to model spot weld failure is to perform a range of mechanical tests to develop an experimental failure locus based on the critical loads that can be readily interpolated in finite-element models. A functional form to describe the failure locus is then assumed and calibrated using the experimental data [23]. Although this approach does not comprehensively account for RSW metallurgical inhomogeneities and provides limited insight into the underlying mechanics of weld failure compared to mesoscale modeling, it is well-suited for industrial application and implementation into finite-element software used for vehicle crash simulation such as LS-DYNA [24]. In this approach, the failure response of spot welds is most commonly characterized under bending-dominated, shear-dominated, and tensile-dominated loads using coach peel [11], lap shear, and cross-tensile tests [7], respectively.

The geometry adopted in the coach peel test can significantly affect the results by changing the severity of bending [25, 26]. The RSW coach peel test typically involves joining two L-shaped coupons with a spot weld on the horizontal flange region. During this test, the weld is subjected to normal tensile stress and bending stress due to the offset between the loading axis and spot weld. Calibration of the RSW failure loci in bending-dominated loading conditions has received limited attention in the available literature due to challenges in determining bending moment using coach peel tests. Complexity arises from the opening of the lower arms and the deformation of the unconstrained vertical arms that do not necessarily remain straight throughout the coach peel test [26]. It is common to idealize the coach peel test and use a constant moment arm which can overestimate the bending moments, as recently reported by Xu et al. [27]. However, with the adoption of digital image correlation (DIC), a more rigorous treatment of the coach peel test can be developed to account for the deformation of the coupon, and better estimate the bending moment, and tensile loads applied to the weld.

RSW failure loci are commonly calibrated in combined shear-tensile loading. Wung [12] proposed the initial form of RSW failure criterion using shear (lap shear) and normal (cross-tensile) tests. A more advanced form of RSW failure

criterion was proposed by Lin et al. [28] that accounted for combined shear and tensile test data obtained from KS-II tests. The KS-II test provides a more favorable boundary condition to characterize weld failure due to the constraint imposed upon the weld in contrast to lap shear tests that can have significant rotation. The calibration of RSW failure models in shear-tensile loading typically assumes the orientation of the coupon is fixed even though coupon rotation can be significant in shear-dominated conditions [13, 29, 30]. Song [31], and Langrand [32] demonstrated how deformation-induced rotations of the weld can lead to major discrepancies between the measured and predicted failure strengths using Lin's failure criterion [33]. The issue of coupon deformation and rotation was acknowledged by Pandya et al. [34] during the combined loading of a 1G-AHSS spot weld using a modified cross-tension fixture that utilized orientation plates to minimize deviation from the intended loading path. Therefore, the construction of a reliable RSW failure locus in shear/tensile loading conditions demands the decomposition of KS-II failure loads into shear and tensile strength components based on the orientation of the nugget at the onset of failure initiation as opposed to the orientation at the start of the test, as discussed by Shojaee et al. [35].

In this study, the validity of existing force-based RSW failure models was evaluated by performing coach peel and KS-II mechanical tests of resistance spot welds under bending-dominated and mixed shear-tensile loading conditions, respectively. Optimized and suboptimal RSW currents were considered to recognize how changing the FZ diameter affects the shape and size of the failure loci. Novel procedures were developed using DIC techniques to improve the characterization of the RSW failure load components by quantifying the orientation of the coupons during the test. The results highlight deficiencies of existing RSW failure models, especially in bending-dominated loading cases where large discrepancies were observed in the shape of the experimental failure locus compared to the convex shape predicted by existing empirical functions. Modified RSW failure functional forms were proposed to accurately predict the failure of 3G-AHSS spot-welded connections in bending-dominated as well as combined shear and tension loading cases.

2 Experimental procedures

2.1 Materials

Two grades of 3G-AHSS were considered, designated 3G-980 and 3G-1180, with nominal ultimate tensile strengths (UTS) of 980 and 1180 MPa, respectively. The steels were uncoated with a nominal thickness of 1.4 mm. Table 1 summarizes the chemical compositions and average tensile properties of the investigated 3G-AHSS in the rolling direction. The equation of Yurioka et al. [36] was used to calculate the carbon equivalent values. The BM uniaxial tensile properties of the same lots of material were characterized by Midawi et al. [17] using JIS Z2201 No. 5 tensile tests with a 50 mm virtual extensometer gauge length.

2.2 Resistance spot welding

RSW was carried out using a robotic medium-frequency direct current (MFDC) welder equipped with a Rexroth Bosch weld controller. 7 mm flat Cu-Cr dome-shaped electrodes were used for spot welding throughout this study. The electrodes were continuously cooled via 20°C water with a nominal flow rate of 6 L/min. RSW process parameters were selected based on the recommendations of the AWS D8.9 standard [37] and their values are outlined in Table 2. To investigate the influence of nugget size on the size of the failure contours, two different nugget diameters were produced for each of the investigated materials: an electrode face diameter weld size (FDWS) of 7 mm and a minimum weld size (MWS) of $4\sqrt{t} \approx 4.7$ mm where t is the thickness of the sheet. The minimum allowable weld size criterion of $4\sqrt{t}$ was chosen based on the guidelines of the AWS D8.1 standard [38]. A weldability window (weld lobe) to produce the FDWS and MWS was developed by changing the welding current from 6.0 to 10.0 kA in 0.1 kA increments. All other process parameters were kept constant. The nugget diameters were measured via cross-sectioning of the welds followed by optical microscopy. Heat inputs as a result of different welding schedules were calculated according to the procedure of Song et al. [39].

Table 1 Chemical composition and mechanical properties of the investigated 3G-AHSS in the rolling direction by Midawi et al. [17]

Material	Mechanical properties					Chemical composition	
	YS [MPa]	UTS [MPa]	TE [%]	UE [%]	n	C_{eq}	C + Mn + Si [wt. %]
3G-980	606	1002	28.1	19.9	0.17	0.64	3.83
3G-1180	993	1230	16.5	10.9	0.09	0.70	4.29

YS yield strength; UTS ultimate tensile strength; TE total elongation; UE uniform elongation; n hardening exponent; C_{eq} carbon equivalent. Mechanical properties are an average of five test repetitions

Table 2 Resistance spot welding process parameters

Material	Squeeze time [ms]	Number of pulses	Weld time for each pulse [ms]	Cool time between pulses [ms]	Hold time [ms]	FDWS Welding current [kA]	MWS Welding current [kA]
3G-980	167	2	167	33	167	9.1	7.0
3G-1180	167	2	167	33	167	9.0	6.9

MWS minimum weld size ($4\sqrt{t} \approx 4.7$ mm fusion zone diameter); FDWS electrode face diameter weld size (≈ 7.0 mm fusion zone diameter)

RSW cross sections were prepared for optical microscopy (OM) following conventional metallographic procedures *i.e.*, rough grinding, fine polishing up to 1 μm polishing diamond paste, and etching with 2% Nital solution. A Keyence VHX digital microscope was used for the FZ diameter measurement of different welding schemes.

2.3 Digital image correlation

All coach peel and KS-II mechanical tests were coupled with stereoscopic digital image correlation analysis for accurate tracking of coupon displacement. A random black-and-white speckle pattern was created in regions of interest for tracking the displacement fields. The DIC system was equipped with a pair of GZL-CL-41C6M-C camera models from Point Grey Research with a 0.005 mm/pixel image scale. VIC 3D R9.1 software from Correlated Solutions was used for the post-processing. A subset size, step size, and strain filter size of 21 pixels, 7 pixels, and 5, respectively, were selected. The weighting of subsets was based on the default Gaussian

weight option and a 90% center-weighted Gaussian strain filter was used. The virtual strain gauge (VSG) [40] was 49 pixels (0.245 mm).

2.4 Coach peel tests to characterize combined bending and tensile loading

Coach peel tests were performed to characterize failure in combined bending and normal loading cases. Three coach peel coupon geometries (shown in Fig. 1) with different initial bending moment arms were considered to achieve different proportions of applied bending moment and tensile loads on the spot welds. The initial bending moment arm is defined as the distance between the center of sheet thickness at the grip (vertical flange) and the projected center of the FZ along the bottom arm (initially horizontal flange region of the coach peel coupon). It is noted that this assumption is expected to underestimate the moment arm length after the peak load as cracks propagate through the weld (interfacial failure (IF)) or around its periphery (pull-out failure

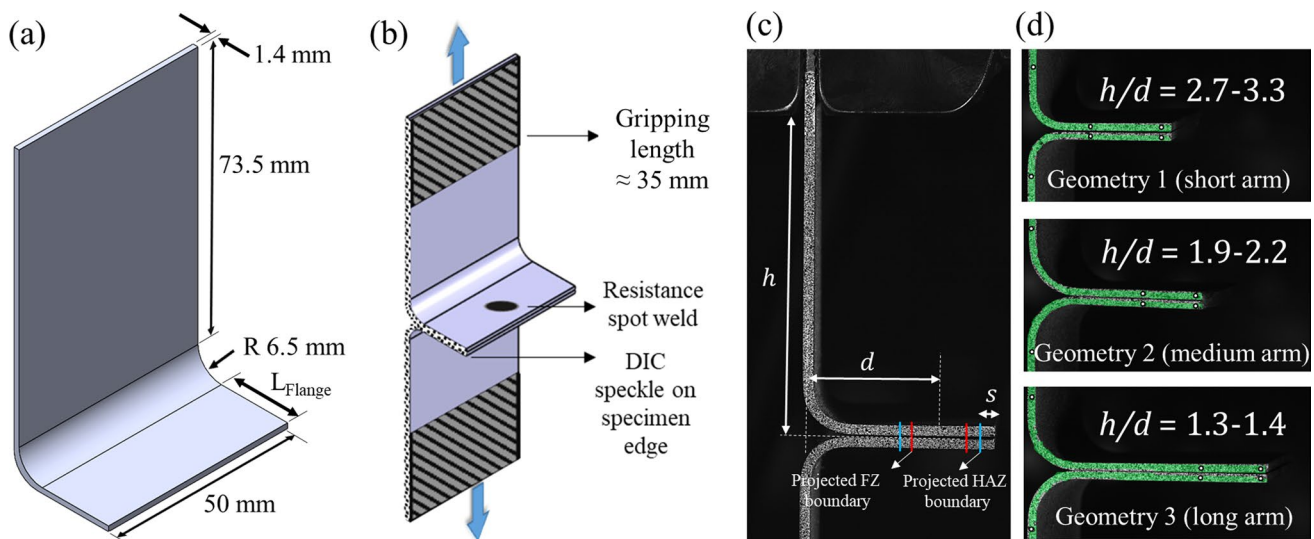


Fig. 1 Schematic representation of (a) coach peel coupon geometry and dimensions, (b) welded coach peel specimen showing the speckled region of interest; (c) “h” is the vertical distance from the grip to the centerline of two sheets; “d” is the horizontal distance from mid-thickness of the sheet at the grip to projected FZ boundary; “s” is the

over-hang distance after the spot weld on the horizontal flange; (d) three different coach peel geometries with various horizontal flange lengths (L_{Flange}) were considered. Dimensions L_{Flange} , h , d , and s are outlined in Table 3 for all three experimented coach peel geometries

(PO)). Coach peel tests were repeated at least 3 times for each welding schedule and geometry. The respective vertical and horizontal arms of the coupon, h , and d (as defined in Fig. 1(c)) were measured individually prior to each test and the average measurements along with the corresponding 95% confidence intervals are outlined in Table 3 for all coach peel geometries and experimented RSW schemes.

In this section, a novel methodology for the coach peel test is proposed that exploits the DIC measurements to account for the deformation and rotation of the arms that affect the evolution of the bending moment, and tensile loads. As an example, the deformation and rotation of the coach peel coupons are shown in Fig. 2 for the 3G-980 FDWS short arm geometry at the initial, peak load, and final frames.

A static equilibrium analysis was conducted on the coach peel coupons to estimate the evolution of bending moment, and tensile force acting on the RSW throughout the tests. The coupon is assumed to be constructed of four rigid beams defined by eight point inspectors (P_1 - P_8) that construct four position vectors $\overline{p_1p_2}$, $\overline{p_3p_4}$, $\overline{p_5p_6}$, and $\overline{p_7p_8}$. Inspectors P_3 , P_4 , P_7 , and P_8 were placed at the edges of the projected RSW FZ, whereas inspectors C_1 and C_2 were placed at the center of the projected FZ. The intersection of vectors $\overline{p_1p_2}$ and $\overline{p_3p_4}$ is referred to as point P_9 . A schematic representation of the undeformed and deformed coach peel coupon, along with the location of point inspectors can be seen in Fig. 3(a) and (b), respectively.

The total opening angle, 2α , is determined by the dot product:

$$\cos(2\alpha) = \frac{\overline{p_3p_4} \cdot \overline{p_7p_8}}{|\overline{p_3p_4}| |\overline{p_7p_8}|} \tag{1}$$

The tensile force applied to the center of the spot weld is equal to the recordings of the vertical load cell ($\vec{F}_{T,RSW} = \vec{F}_{Loadcell}$). The effective bending moment arm (\vec{d}_e) is defined as the instantaneous horizontal distance between inspector P_1 at the mid-thickness of the upper arm at the grip and inspector C_1 located at the projected center of the spot weld. The bending moment imposed upon the weld, \vec{M}_{RSW} , can be defined using the tensile force applied to the center of spot weld ($\vec{F}_{T,RSW}$) and the effective moment arm, \vec{d}_e :

$$\vec{M}_{RSW} = \vec{d}_e \times \vec{F}_{T,RSW} \tag{2}$$

It is noted that any compressive contact between the lower arms due to the overhang distance, s , has been ignored. The overhang distance should be minimized with distances between 4.5–7.2 mm in the present study as outlined in Table 3.

Examples of the evolution of parameters \vec{d}_e , α , \vec{M}_{RSW} , and $\vec{F}_{T,RSW}$ have been summarized for a 3G-980 FDWS

Table 3 Summary of average horizontal flange length (L_{Flange}), initial bending moment arm on the horizontal arm “d”, initial bending moment arm on the vertical arm “h”, and free overhang distance (s) for 3 different coach peel coupon geometries and 4 different welding schemes investigated in this study. Errors are 95% confidence interval values

Welding condition	Geometry 1 (short arm)				Geometry 2 (medium arm)				Geometry 3 (long arm)			
	L_{Flange} [mm]	d [mm]	h [mm]	s [mm]	L_{Flange} [mm]	d [mm]	h [mm]	s [mm]	L_{Flange} [mm]	d [mm]	h [mm]	s [mm]
3G-980 FDWS	19.5	12.8 ± 1.2	42	6.0 ± 2.1	25	22.1 ± 0.1	42.5	4.5 ± 0.8	32	31.4 ± 0.3	41	4.9 ± 0.9
3G-980 MWS	19.5	15.4 ± 1.2	42	7.2 ± 1.8	25	21.2 ± 0.1	42.5	5.0 ± 0.6	32	31.4 ± 0.5	42	4.5 ± 0.5
3G-1180 FDWS	19.5	13.2 ± 0.8	42.5	6.3 ± 1.5	25	20.4 ± 0.2	42.5	4.6 ± 0.7	32	31.3 ± 0.2	42	4.8 ± 0.7
3G-1180 MWS	19.5	13.4 ± 1.6	42	6.8 ± 1.9	25	19.3 ± 0.2	42.5	5.1 ± 0.3	32	30.4 ± 0.1	42.5	5.0 ± 0.6

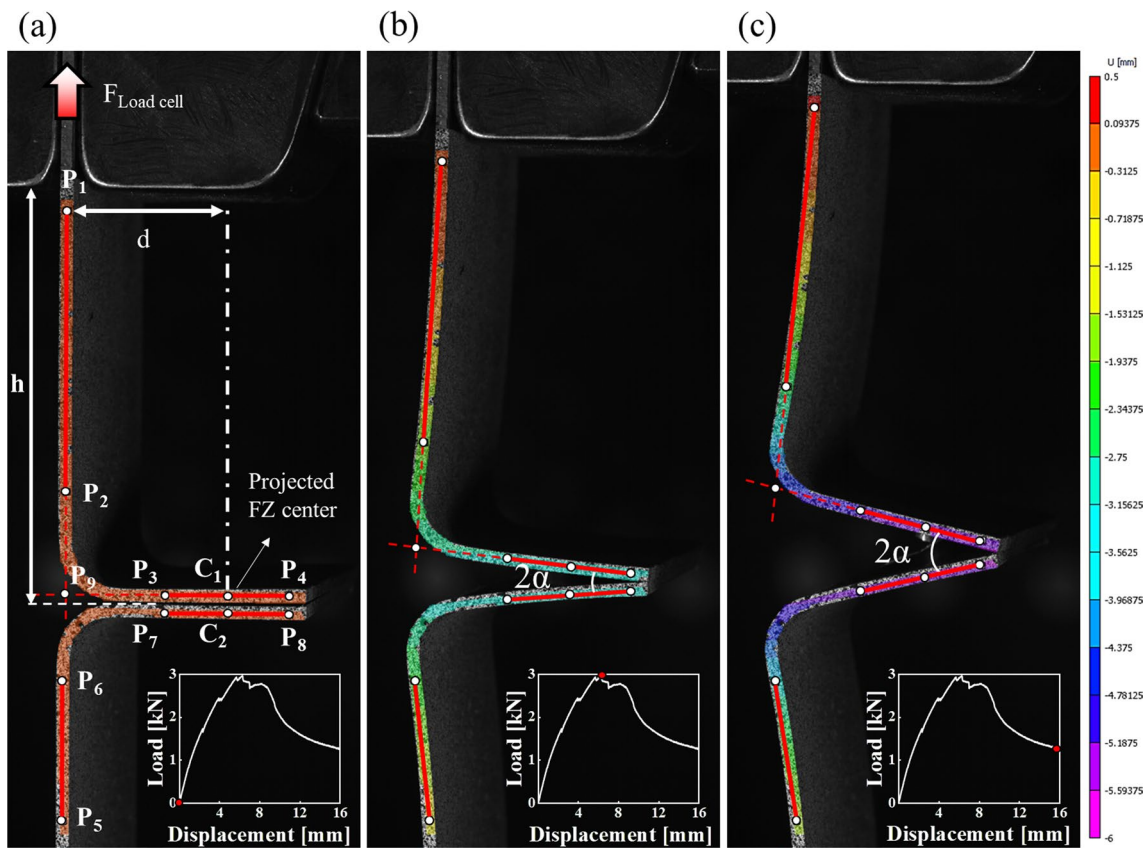
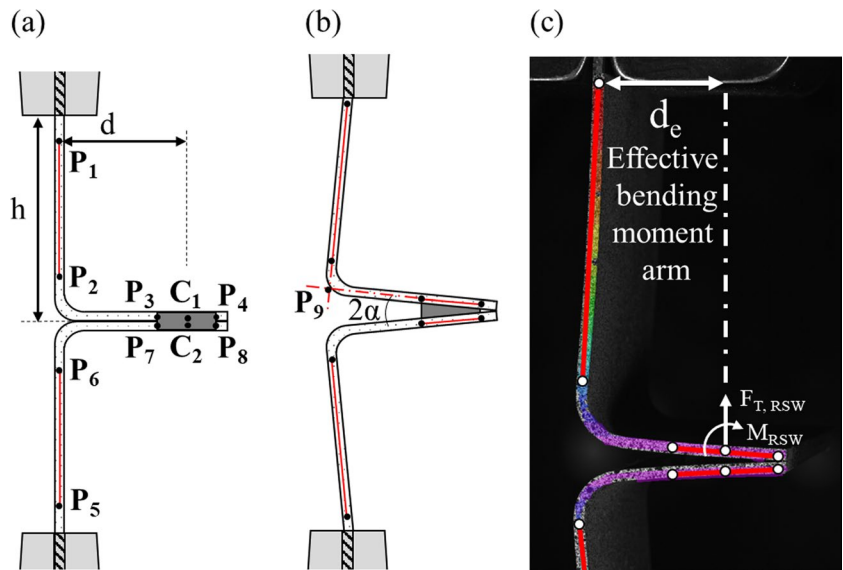


Fig. 2 Comparison between (a) first, (b) peak load, and (c) final frame of a short arm (geometry 1) 3G-980 FDWS coach peel test. Figures highlight the deformation of the coupons and the continuous

reduction of the effective bending moment arm acting on the projected FZ center throughout the test. The color contour U shows horizontal displacement within the region of interest

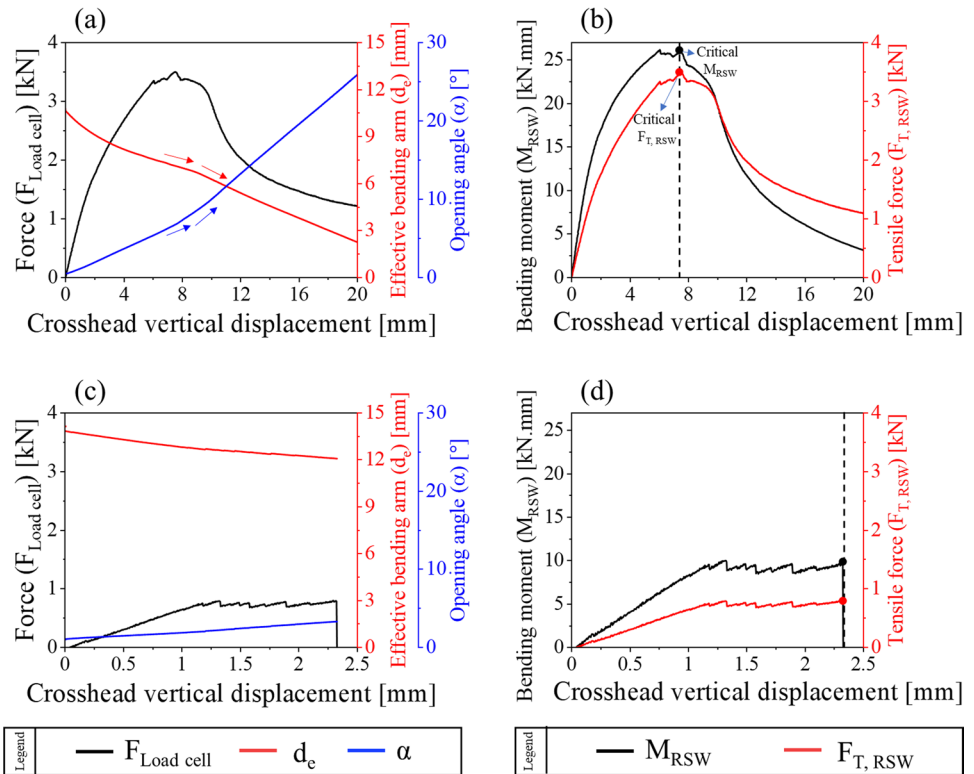
Fig. 3 Schematic drawing showing the configuration of the coach peel specimen (a) at the beginning of the test, and (b) n^{th} frame after starting the test. (c) Forces and moments acting at the center of the spot weld



and 3G-980 MWS geometry 1 (short arm) coach peel test. Figure 4(a) illustrates how the effective bending moment arm decreased by 34% and 76% from the beginning of a

3G-980 FDWS short arm coach peel test up to the peak load, and final frame, respectively. It was observed that the bending arm reduces at a higher rate after the critical

Fig. 4 Representative evolution of effective bending moment arm (d_e), opening angle (α), bending moment (M_{RSW}), and tensile force ($F_{T,RSW}$) applied to the projected RSW FZ throughout (a) and (b) 3G-980 FDWS, and (c) and (d), 3G-980 MWS geometry 1 (short arm) coach peel tests



peak load point, as highlighted by the steeper slope of the red arrow in Fig. 4(a) after the peak load point. The higher reduction rate in the bending moment arm can be correlated with the detachment of an RSW leg during PO failure of the FDWS condition, which facilitates out-of-plane rotation of the nugget during the unloading stage of the test. In the case of the 3G-980 MWS short arm coach peel test, as shown in Fig. 4(c), changes in the effective bending arm were less severe with a 13% reduction until peak load by the end of the test. The alteration in the bending arm is less significant in the MWS condition due to the limited deformation of the coupons prior to full separation in IF mode. The observed trends clearly highlight the need to consider the evolution of the bending moment during coach peel tests for the accurate generation of fracture models. Alteration of the forces and moments effective on the spot weld for the same 3G-980 FDWS and 3G-980 MWS short arm coach peel tests are shown in Fig. 4(b) and (d), respectively. The corresponding critical bending, and normal force values at the onset of separation, defined by the peak load, were determined for all tests, and the values were used to evaluate the existing RSW failure prediction models in tensile load-bending moment conditions outlined in Sect. 3.5.

Upon determining the evolution of load components, the tensile energy absorption capacity of the spot weld ($E_{T,RSW}$) is calculated as:

$$E_{T,RSW} = \int F_{T,RSW} \cdot \delta t_{C1-C2} \tag{3}$$

where δt_{C1-C2} is the relative vertical displacement of the projected FZ center, tracked via the displacement field of inspectors C_1 and C_2 . The vertical crosshead displacement does not accurately reflect the displacement of the nugget on the bottom horizontal flange region, as evidenced via the arm deformations and nugget rotation shown in Fig. 2. Therefore, the evolution of $F_{T,RSW}$ parameters were plotted against the local relative displacements at the projected centers of the FZ on the upper and lower coach peel coupons, rather than the global crosshead vertical displacement. Considering the local displacement field minimizes the influence of deformations occurring at regions away from the spot weld on the subsequent $E_{T,RSW}$ calculations. The moment energy ($E_{M,RSW}$) due to rotation of the nugget (opening angle $\delta\alpha$) is defined as:

$$E_{M,RSW} = \int M_{RSW} \cdot \delta\alpha \tag{4}$$

The total joint absorbed energy ($E_{Total,RSW}$) is defined as the sum of $E_{T,RSW}$, and $E_{M,RSW}$. $E_{Total,RSW}$ were compared against global energy dissipation values (E_{Global}) calculated from the area under crosshead vertical displacements- $F_{Load\ cell}$ plots.

2.5 KS-II tests to characterize combined shear and tensile loading

In this study, KS-II tests for MWS conditions were performed in 8 orientations to obtain a broad range of shear-tensile loading ratios. The KS-II test results for the FDWS condition were reported in a previous study by the authors [35] and are used to contrast with the current MWS condition. Figure 5(a) and (b) illustrate the KS-II coupon geometry with the spot weld located at the center of the mating surfaces. The instantaneous loading angle, θ , is defined as the angle between the load application line from the tensile frame and the plane of contact between the two coupons. A custom-designed fixture based on the butterfly apparatus [41] was used to impose different combinations of shear and tensile loads on the investigated spot welds (Fig. 5(c)). The KS-II fixture consisted of a pair of KS-II holder assemblies as shown in Fig. 5(d). The KS-II specimen is attached to the holder assembly via spacers. Upon clamping the KS-II specimens within the fixture, the frame assembly is loaded in tension via two pins, one attached to the upper movable actuator and the other fixed to the stationary bolster of a 100 kN servo-hydraulic displacement-controlled tensile machine. All KS-II tests were performed at a constant 10 mm/min crosshead speed rate to minimize dynamic loading effects. By rotating the holders, it was possible to achieve Mode I opening ($\theta = 90^\circ$), Mode II shearing ($\theta = 0^\circ$), and mixed mode loading orientations ($\theta = 10^\circ, 15^\circ, 30^\circ, 45^\circ, 60^\circ,$ and 75°). The schematic in Fig. 6 shows the shear and tensile components of forces acting on the spot welds in different orientations of the KS-II tests. The KS-II tests were intended to load the spot weld in shear (0° loading orientation), and incrementally add the tensile component of the force until 90° loading orientation. The peak loads were extracted from the load cell data output. All reported values for KS-II peak loads and coupon rotations are an average of 5 tests and the error bars are 95% confidence intervals.

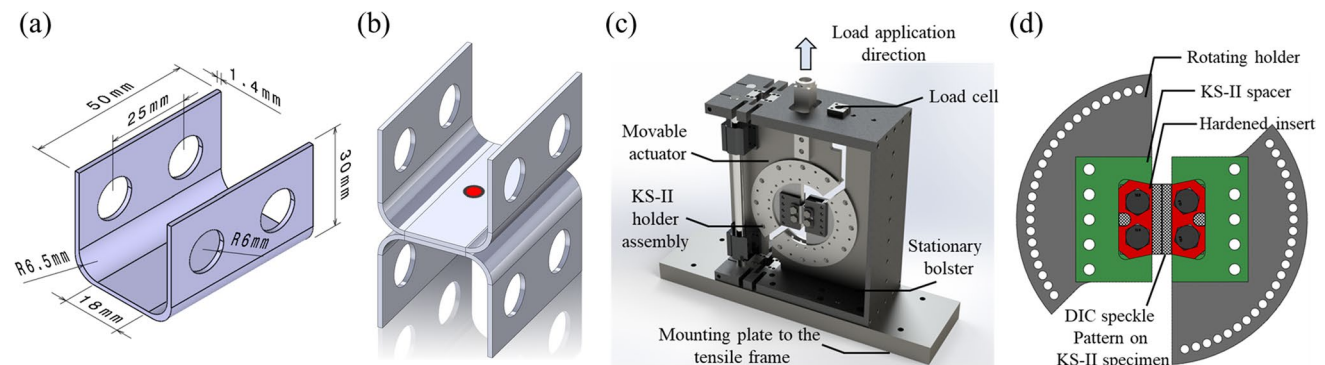


Fig. 5 **a** Schematic representation of KS-II coupon geometry and dimensions; **b** welded KS-II specimen; **c** assembled KS-II testing fixture capable of applying loads in 5° loading angle increments; **d**

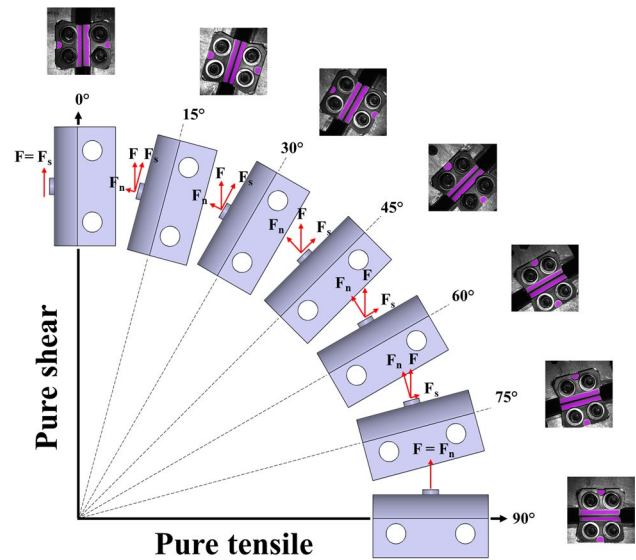


Fig. 6 Schematic representation of different KS-II loading orientations showing the shear and tensile components of force acting on the spot welds. (Loading in 10° orientation not shown for clarity)

Figure 7 shows the first and final images related to the displacement fields that were tracked for a KS-II test at 10° loading orientation. DIC circle inspector tools with a 2.5 mm diameter were used to report the displacement in the KS-II tests. The location of the point and circular inspectors is shown in Fig. 7 as well. The opening windows in the KS-II inserts, where C_0 and C_3 inspectors are located, were machined to account for any asymmetric deformation of the two coupon halves. The displacement of point C_0 was shown in a previous study to accurately represent the crosshead displacement [35].

Examining the KS-II DIC images revealed a non-negligible amount of slippage throughout some of the KS-II tests, especially in the shear-dominated orientations of $0^\circ, 10^\circ, 15^\circ,$ and 30° . Most of the slippage occurs at the coupon level due to

detailed view of the KS-II specimen holder assembly comprised of KS-II specimen, spacer, inserts, and rotating holder

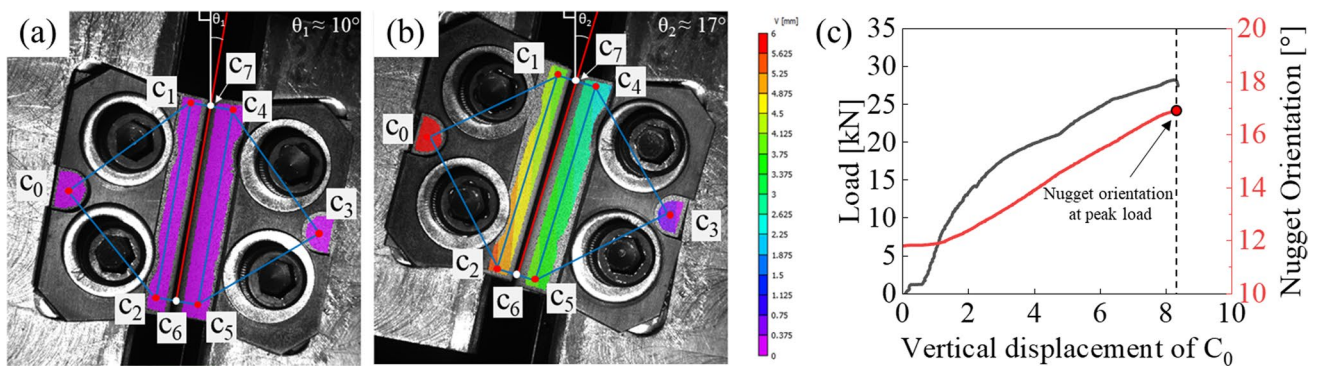


Fig. 7 Comparison between (a) first and (b) final frame of a KS-II test at 10° loading orientation. The color contour V represents vertical displacement within the region of interest. (c) load-displacement

and nugget orientation plot of the same test shows the instantaneous orientation of the nugget throughout the test

the clearance holes not being completely engaged with the KS-II holder at the beginning of the tests. Any slippage or induced rotation of the KS-II specimen within the grip must be accounted for to correctly resolve the shear and tensile force components. For example, Fig. 7(a) and (b) demonstrate how a KS-II specimen, with an approximate initial 10° loading orientation, rotates by approximately 7° before full detachment (failure) of the coupon by the end of the test. The methodology for approximation of the actual nugget orientation consisted of using 6 circular point inspectors within the DIC region of interest to form two triangles, the vertices of which track the non-symmetric orientation of each coupon half independently. In this approach, points C₆ and C₇ construct a line between the two KS-II coupon halves that contain the nugget, and the instantaneous slope of this line is updated as the current orientation of the nugget. The respective shear and tensile force components, \vec{F}_s and \vec{F}_n , are related to the measured force at the load cell, $\vec{F}_{Loadcell}$, as:

$$|\vec{F}_n| = |\vec{F}_{Loadcell}| \times \sin(\theta) \tag{5}$$

$$|\vec{F}_s| = |\vec{F}_{Loadcell}| \times \cos(\theta) \tag{6}$$

Additional details on the KS-II post-processing procedure can be found elsewhere [35].

3 Results and discussion

3.1 Weld characteristics

The welding schedules reported in Table 2 were selected to create FDWS and MWS nuggets in the investigated steels. Figure 8 shows a cross-sectional view of the welded samples along with a comparison of the total heat input. Generally, the 3G-1180 steel exhibited a higher rate of nugget growth, due to its higher alloying content, as reflected in the carbon equivalent values reported in Table 1. A detailed discussion on sub-zone microstructures that are formed, their hardness, and the stress-strain curves of different HAZ and FZ for the same material can be found elsewhere [17, 42].

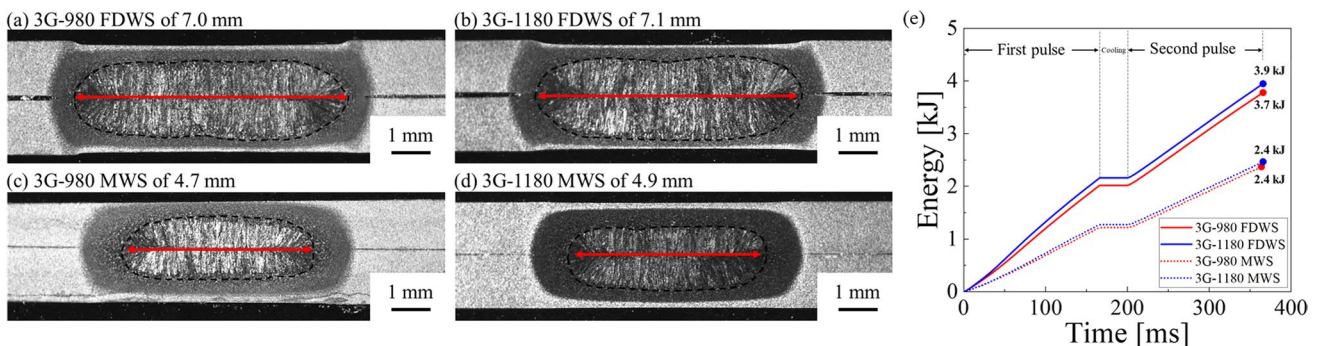


Fig. 8 Optical images of RSW cross sections for (a) and (b) electrode face diameter weld size (FDWS), (c) and (d) minimum allowable weld size (MWS) illustrating the fusion zone diameters. (e) accumu-

lated energy vs time graph representing heat input as a result of different welding schemes

3.2 Coach peel test results

Representative evolution of parameters $F_{T,RSW}$, and M_{RSW} during testing three geometries of coach peel specimens have been illustrated for different welding schemes in Fig. 9. Results revealed that the spot welds fail under a combination of bending moments and tensile-dominated forces in the coach peel testing geometry. The initial bending arm (d) was increased between 188 to 213% from the short arm geometry to the long arm geometry of various welding schemes (as reported in Table 3). On average, the increase in the initial bending arm resulted in 215% and 233% increase in displacement-to-failure of 3G-980 and 3G-1180 FDWS test conditions, respectively. The increase of the average failure displacement was 80% and 53%, for 3G-980 and 3G-1180 MWS conditions, respectively. The larger increase in the displacement to failure of the FDWS conditions with larger bending arms is attributed to a transition to a PO failure mode with a larger rotation of the nugget in contrast to the MWS conditions with IF. Furthermore, the long arm conditions exhibited increased plastic deformation of the flange.

The applied force and displacement-to-failure provide limited insight into the performance of the weld in the coach peel test. The severity of the applied bending moment is a function of the geometry and its evolution during the test. Therefore, the evolution of the bending moment and tensile forces were plotted against their corresponding displacements/rotations for the different coach peel coupon geometries. Subsequently, the load-bearing capacity and energy absorption capability of the welds are calculated independently in tensile and bending conditions.

The average critical $F_{T,RSW}$, and M_{RSW} applied to the projected center of the RSW FZ for all coach peel geometries and welding schemes are shown in Fig. 10. As expected, a decreasing trend in terms of peak load was observed with increasing moment arm length. The suboptimal MWS welds' strength was found to be more sensitive to changes in the coach peel coupon geometry as their average strength decreased between 40 to 65% from geometry 1 (short arm) to geometry 3 (long arm) for 3G-980 and 3G-1180, respectively, compared to a 39% to 41% drop in average peak load for 3G-980 and 3G-1180 FDWS weld conditions. Changing the coach peel geometry from short arm to long

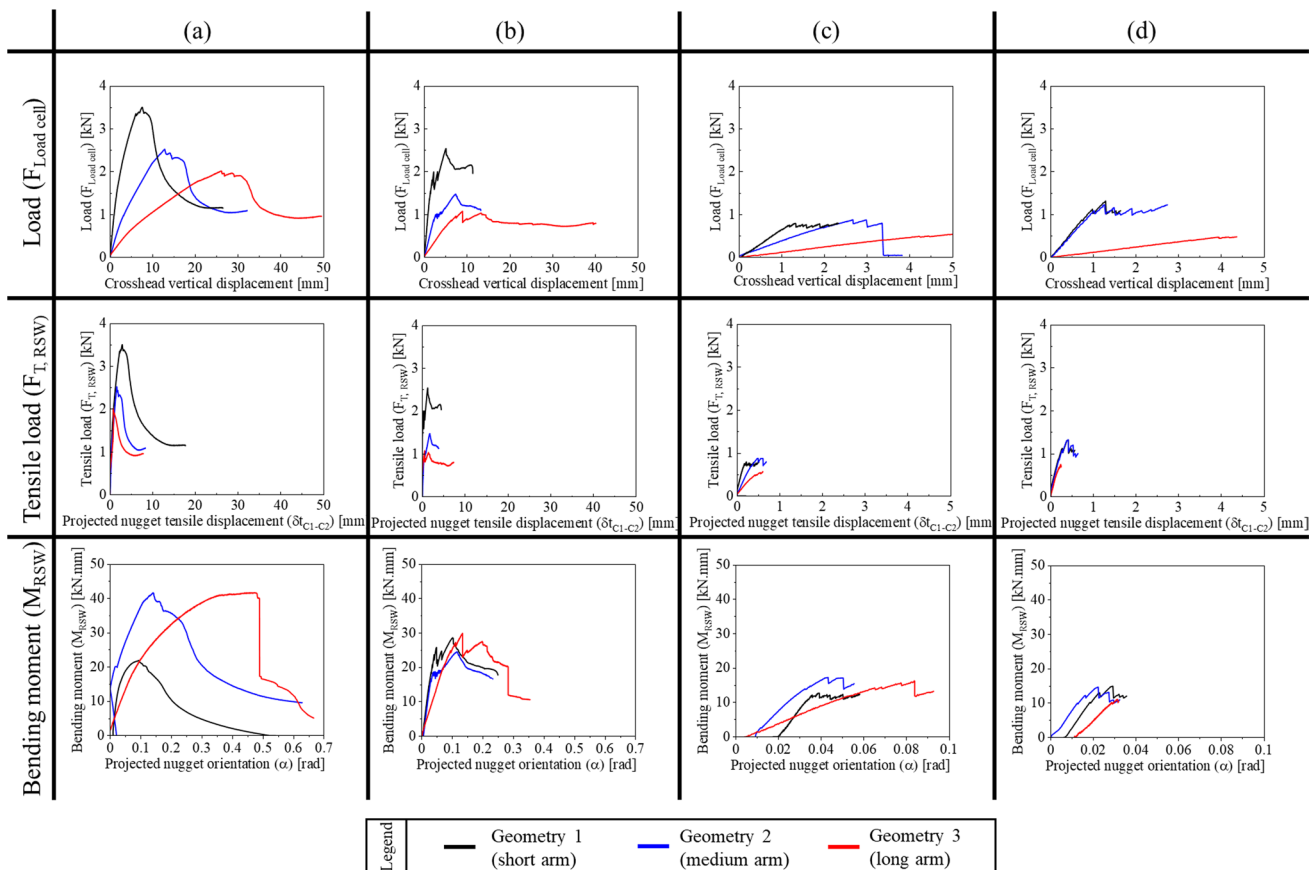
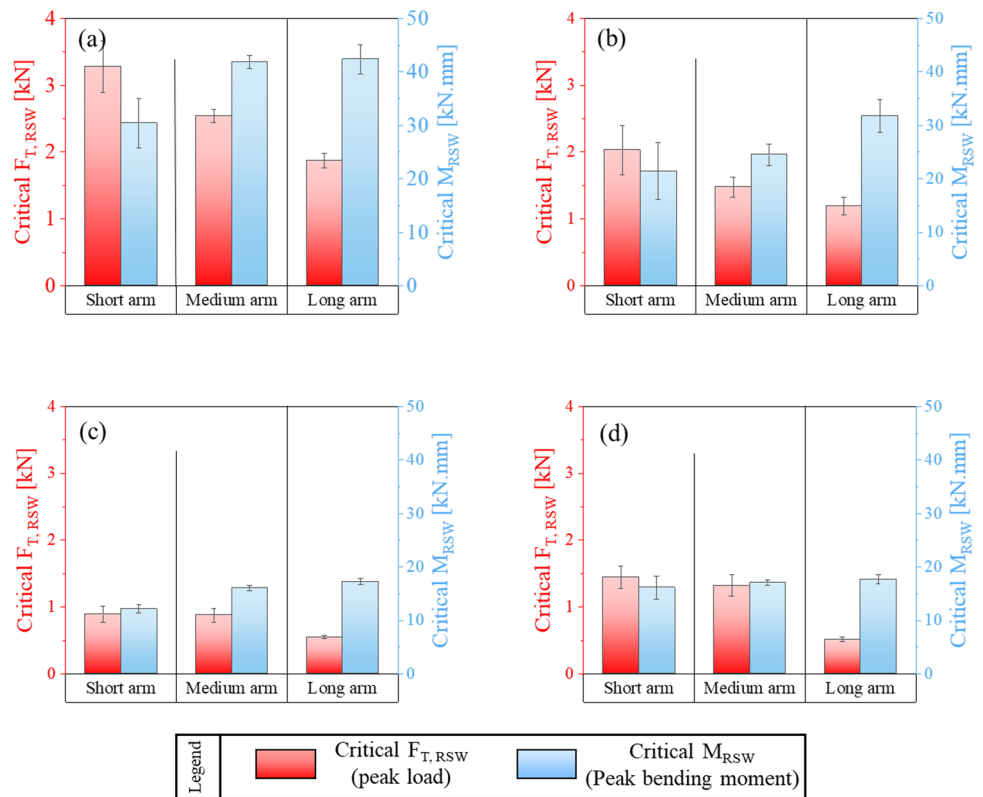


Fig. 9 Representative plots showing the evolution of $F_{Load\ cell}$, $F_{T,RSW}$, and M_{RSW} during testing of three different coach peel geometries of (a) 3G-980 FDWS, (b) 3G-1180 FDWS, (c) 3G-980 MWS, and (d) 3G-1180 MWS welding schemes

Fig. 10 Influence of coach peel coupon geometry on average critical $F_{T,RSW}$ and M_{RSW} applied to the projected center of the RSW FZ for (a) 3G-980 FDWS, (b) 3G-1180 FDWS, (c) 3G-980 MWS, and (d) 3G-1180 MWS welding conditions



arm consistently resulted in a higher average critical M_{RSW} value. The increase in critical M_{RSW} from short arm to long arm geometry was 39% and 49% for 3G-980 FDWS and 3G-1180 FDWS, on average. The increase in M_{RSW} of MWS conditions was calculated at 42% and 10% for 3G-980 and 3G-1180, respectively. It is noted that an idealized assumption of a constant bending arm throughout coach peel tests would have resulted in consistent over-estimation of the critical M_{RSW} values between 74%-138% for FDWS conditions, and between 6%-46% over-estimation for MWS conditions.

The alteration in $E_{T,RSW}$, $E_{M,RSW}$, $E_{Total,RSW}$, and E_{Global} due to changes in initial bending arm length is summarized in Fig. 11. It is interesting to note that the $E_{Total,RSW}$ was relatively unchanged with the change from short to long arm with an 8.1% and 4.5% increase on average for 3G-980 and 3G-1180 FDWS cases. Although the total energy absorption capacity of the joints remained nearly the same, the $E_{T,RSW}/E_{Total,RSW}$ ratio decreased from 69.5% to 35.4% for 3G-980 FDWS, and from 62.6% to 45.1% for 3G-1180 FDWS cases. At the same time, increasing the bending arm from short arm to long arm geometry increased the $E_{M,RSW}/E_{Total,RSW}$ ratio from 30.5% to 64.6% for 3G-980 FDWS, and from 37.4% to 54.9% for 3G-1180 FDWS condition. The $E_{Total,RSW}$ calculations for MWS conditions revealed much more limited energy absorption capabilities as evidenced by the smaller scales in Fig. 11(c) and (d). The larger variation in MWS $E_{Total,RSW}$ is attributed to a few tests

having P-PO failure modes with small plug ratios. Unlike the FDWS conditions, increasing the initial bending arm in MWS welding schemes did not result in a consistently higher $E_{M,RSW}/E_{Total,RSW}$ ratio.

Changes in the effective bending arm (d_e) from the beginning of the test ($d_e = d$) until the peak load frame of the tests were measured according to the procedure outlined in Sect. 2.4 and is summarized in Fig. 12. The reduction in d_e was most noticeable for high heat input FDWS cases. More specifically, the 3G-980 and 3G-1180 FDWS exhibited between 26%-28%, and 16%-22% reduction in d_e , respectively, throughout the three coach peel geometries. The higher reduction in the bending arm of 3G-980 FDWS could be explained by the higher ductility of the as-received steel as well as the tougher behavior of the welds. As an example, representative fracture surfaces along with the cross-sectional view of the short arm FDWS conditions are shown for both investigated materials in Fig. 13. The failure was accompanied by crack initiation and propagation in both materials. While the cracks initiated at the notch tip area on the side closer to the loading axis for both steels, two distinctly different propagation paths were observed between the 3G-980 and 3G-1180 spot welds. In the case of the 3G-980 welds, the cracks immediately grew outwards from the notch and towards the BM region with ductile failure behavior and the development of a neck in the failed joint leg (Fig. 13(a)). After going through the sheet

Fig. 11 Influence of coach peel coupon geometry on average $E_{T, RSW}$, $E_{M, RSW}$, $E_{Total, RSW}$ of the projected center of the RSW FZ, and E_{Global} for (a) 3G-980 FDWS, (b) 3G-1180 FDWS, (c) 3G-980 MWS, and (d) 3G-1180 MWS welding conditions

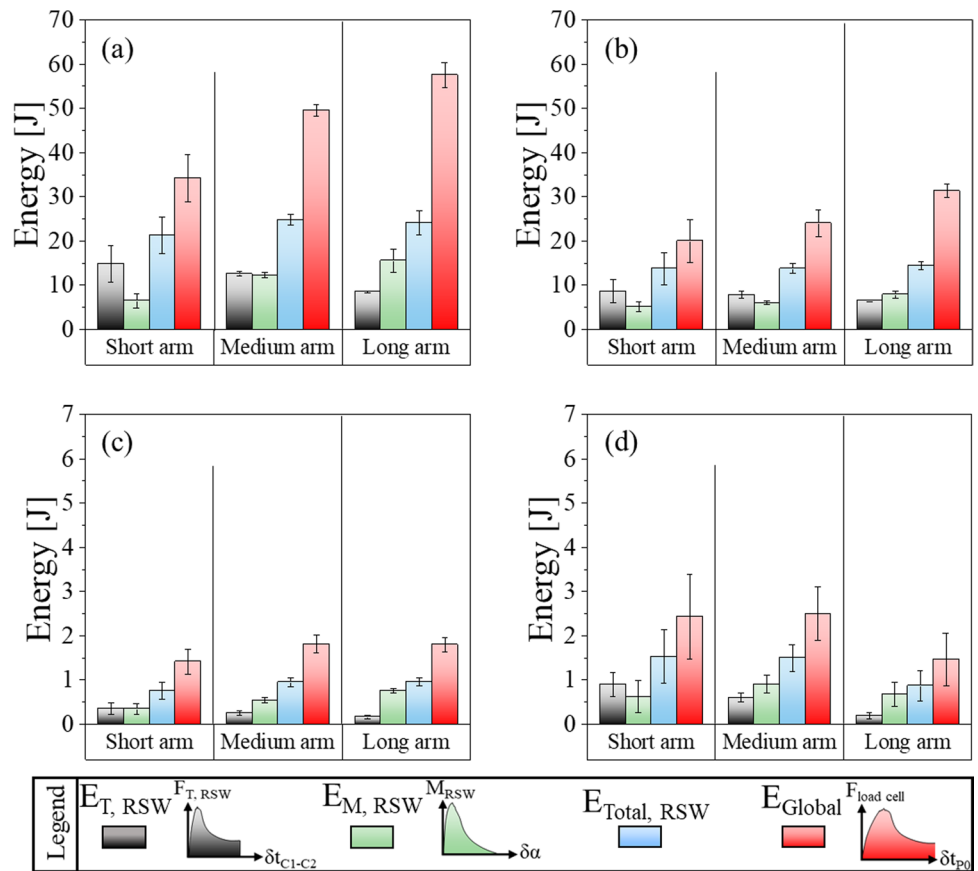
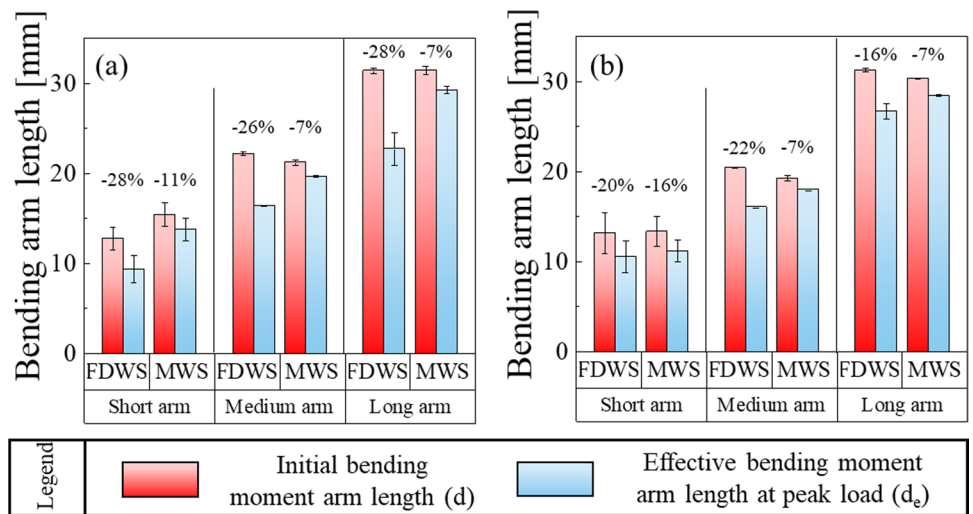
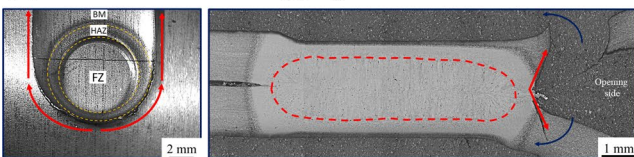


Fig. 12 Changes in effective bending moment arm from the beginning of the tests up to the peak load frame of (a) 3G-980, and (b) 3G-1180 coach peel tests with various geometries and welding schemes



(a) 3G-980 FDWS full nugget pullout



(b) 3G-1180 MWS partial interfacial partial pullout

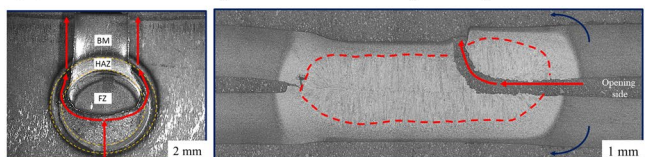


Fig. 13 Representative failure behavior of coach peel geometry 1 (short arm) tests for (a) 3G-980 FDWS and (b) 3G-1180 FDWS conditions

thickness and reaching the faying surface, the cracks grew around the nugget circumference, leaving both the FZ and HAZ intact after full failure. However, in the case of the 3G-1180 (Fig. 13(b)), the cracks rapidly propagated halfway into the FZ, after which the propagation direction switched away from the faying surface. Finite element modeling by Pawar et al. [43] revealed full nugget PO failure of spot welds can accommodate more plastic deformation of the coupons. Therefore, other than the difference in the ductility of the tested 3G-AHSS, the observed failure mechanisms are also believed to be a contributing factor for a more severe reduction in the effective bending arm of the 3G-980 FDWS coach peel tests as compared to the 3G-1180 FDWS tests. Reduction of d_e for various coach peel geometries of 3G-980 MWS and 3G-1180 MWS conditions was between 7%-11%, and 7%-16%, respectively. The differences in the reduction of d_e between the two 3G-AHSS MWS spot welds were determined to be statistically insignificant, which can be correlated with their similar IF behavior in the majority of the tests.

3.3 KS-II test results

Figure 14(a) and (b) show representative measured load–displacement curves for each of the FDWS loading

orientations. The area under the load–displacement curves is typically used as a quality index reflecting the energy absorption capability of the joints. It is observed that the spot welds exhibit much higher strength for shear-dominated loading orientations with limited energy absorption after reaching the peak load value, taken as the onset of failure, as demonstrated by the abrupt unloading response. In contrast, the tests performed under tensile-dominated loading orientations exhibit relatively lower strength values, however, their post-failure energy absorption represents a higher proportion of the total energy absorption, as evidenced by the elongated unloading tails of the corresponding curves. The same overall trends were also observed in the MWS condition as shown in Fig. 14(c) and (d).

The peak load values from each of the tests were extracted for different loading orientations and the corresponding values are plotted in Fig. 15(a) and (b) for FDWS and MWS conditions, respectively. The decreasing trend as loading orientation changes from shear loading (0°) to tensile loading (90°) is related to changes in the stress state at the nugget periphery. In summary, the load-carrying capacity of 3G-980 and 3G-1180 spot welds decreased by 65% and 81% for the FDWS, and 79% and 78% for MWS conditions as the loading orientation changed from 0° to 90° .

Fig. 14 Representative KS-II load-crosshead displacement plots for different loading orientations of (a) 3G-980 FDWS, (b) 3G-1180 FDWS, (c) 3G-980 MWS, and (d) 3G-1180 MWS conditions

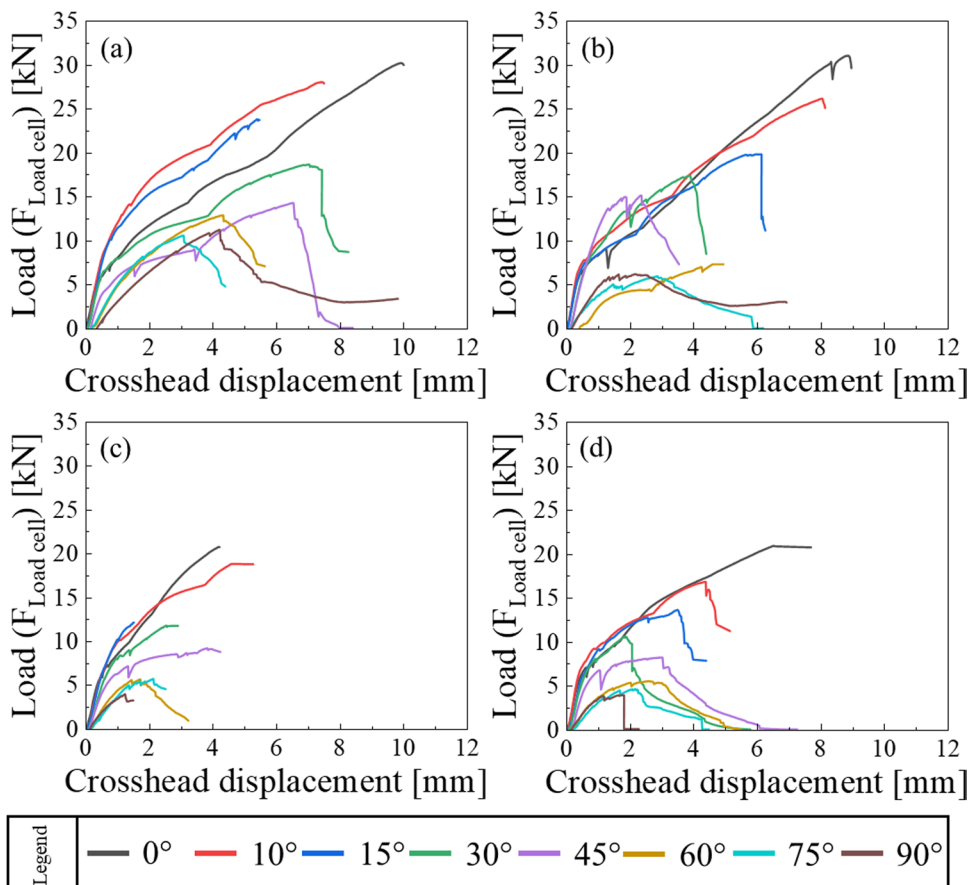
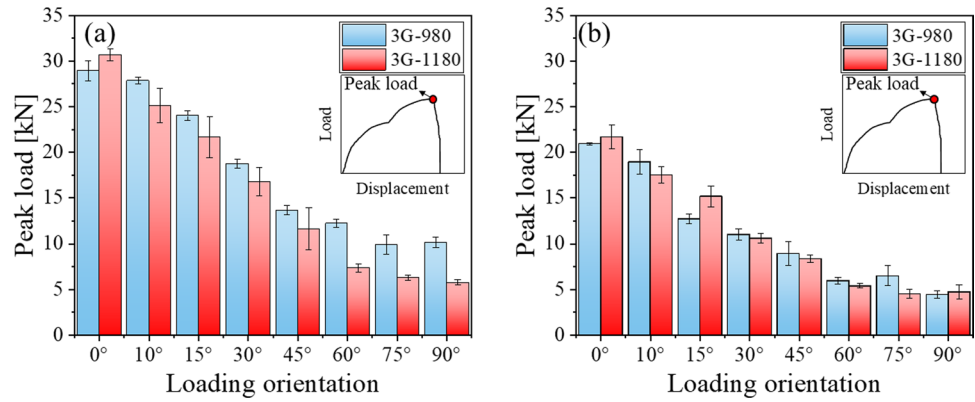


Fig. 15 Influence of KS-II loading orientation on peak load of (a) FDWS and (b) MWS welding schemes



Although the nominal orientation of the nugget is commonly used to calculate the shear and tensile force components [11, 44, 45], the DIC displacement measurements revealed rotations that must be considered. Figure 16(a) summarizes the procedure that was followed for the calculation of the final nugget orientation at the peak load value throughout all performed KS-II loading orientations. As expected, rotations are minimal in tensile-dominant loading orientations (45°–90°). In contrast to uniaxial tension, rotations are unavoidable due to the induced moment in the shear-dominant loading cases. The induced coupon rotation leads to an evolution of the shear and tensile loading components that must be considered in the construction of the RSW failure loci in shear-tensile loading.

3.4 Calibration of existing RSW failure models

Constructing a failure locus for resistance spot welds requires the decomposition of the critical load value into its tensile and shear components at the onset of failure. Identifying the critical failure load in RSW mechanical tests can be challenging due to the weld being hidden and the typically jagged nature of the resultant force–displacement

curves. Local strength drops in force–displacement curves are well documented in the literature and are thought to be due to the slipping of coupons/testing fixtures or the formation of cracks that have not reached critical lengths for further growth [7]. Although some studies have shown crack initiation and partial propagation from the intrinsic notch region in between the welded sheets during the strain hardening (loading) region of the load–displacement curves [46], the peak load point is typically considered the critical failure load.

Different models have been proposed to describe the failure behavior of resistance spot welds. The phenomenological function of Seeger et al. [29] to describe the quasi-static RSW failure locus in tensile-shear loading cases is defined as:

$$f^S = \left[\frac{F_s}{S_S} \right]^a + \left[\frac{F_n}{S_N} \right]^b \leq 1 \tag{7}$$

where the S_S and S_N are the corresponding failure strengths from KS-II samples loaded at 0° (shear) and samples loaded at 90° (tensile), respectively. The exponents a and b are optimized using a least squares regression. The elliptical model

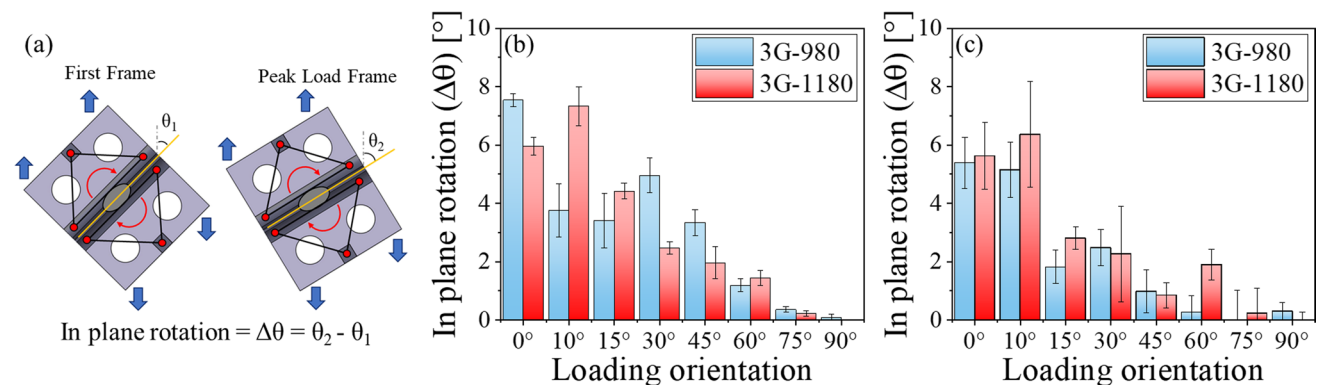


Fig. 16 (a) Summary of procedure for calculating in-plane rotation using DIC data (rotation of the coupons is exaggerated for better visualization of changes in θ). In-plane rotation values at peak load frame for (b) FDWS and (c) MWS conditions

of Lee et al. [47], denoted f^L , is a special case of the Seeger model with $a=b=2$.

Song and Huh [31] proposed an alternate elliptical model:

$$f^{SH} = \left[\frac{F_n}{S_N} \right]^2 + \varphi \left(\frac{F_n}{S_N} \right) \left(\frac{F_s}{S_S} \right) + \left[\frac{F_s}{S_S} \right]^2 \leq 1 \tag{8}$$

where φ is a shape parameter. This failure contour takes the form of f^L if $\varphi = 0$ and becomes a straight line when $\varphi = 2$.

The three models were calibrated and the corresponding calibrated failure loci in shear-tensile loading conditions are shown in Fig. 17(a) and (b) for 3G-980 and 3G-1180 spot welds, respectively. Seeger’s two-dimensional model (Eq. 7), with its two shape exponents as variables, provided the best agreement with the experimental data with an average of between 0.2% to 3.5% over-prediction error. Figure 17(c) outlines the average error of different model predictions compared to the experimental failure load components upon using the triangular KS-II analysis. It is observed that the Song and Huh model underestimates the failure strength of the investigated 3G-AHSS spot welds between 9.2% and 22.3% on average for all orientations. The average error of under-predictions drops to between 0.4% and 3.7% for Lee’s model. It appears the quadratic constraint of f^L and f^{SH} models is overly restrictive with poor predictions in combined tension and shear. Consequently, the more flexible f^S model is selected as a basis for comparison and further analysis of the existing RSW loci failure predictions.

Seeger et al. extended Eq. 7 to a three-dimensional surface to account for bending [48]:

$$f^S = \left[\frac{F_s}{S_S} \right]^a + \left[\frac{F_n}{S_N} \right]^b + \left[\frac{M_b}{S_B} \right]^c \leq 1 \tag{9}$$

in which S_B is the critical bending moment applied to the spot weld at the onset of failure during coach peel tests. Failure is predicted to occur when Eq. 9 exceeds unity, corresponding to loading outside of the failure surface. Wang et al. [23] proposed determining S_B by assuming the polynomial-based failure surface as

$$S_B = \frac{F_{MaxCP} \times d}{\sqrt{1 - \left(\frac{F_{MaxCP}}{F_{MaxKS-II90^\circ}} \right)^2}} \tag{10}$$

where $F_{Max, CP}$, and $F_{Max, KS-II 90^\circ}$ are the maximum load-bearing capacities in coach peel and KS-II at 90° tests, respectively, and d is the initial bending moment arm of a single coach peel geometry. The appropriate value of c in Eq. 9 cannot be determined with a single coach peel geometry and is conventionally assumed that $c=2$ [29, 49]. The predicted three-dimensional failure surfaces of Seeger in Eq. 9 with the value of S_B determined from Eq. 10 based on peak load data from the short arm coach peel geometry are shown in Fig. 18. The calibrated force-based failure strengths and exponents have been summarized in Table 4.

The following two sections focus on assessing the accuracy of failure strength predictions from Seeger’s model shown in Fig. 18. More specifically, the experimentally acquired failure data, summarized in Sections 3.2 and 3.3, are contrasted with Seeger’s model in shear-tensile and tensile-bending loading conditions (dashed black lines in Fig. 18). Suitable alternative functional forms are proposed

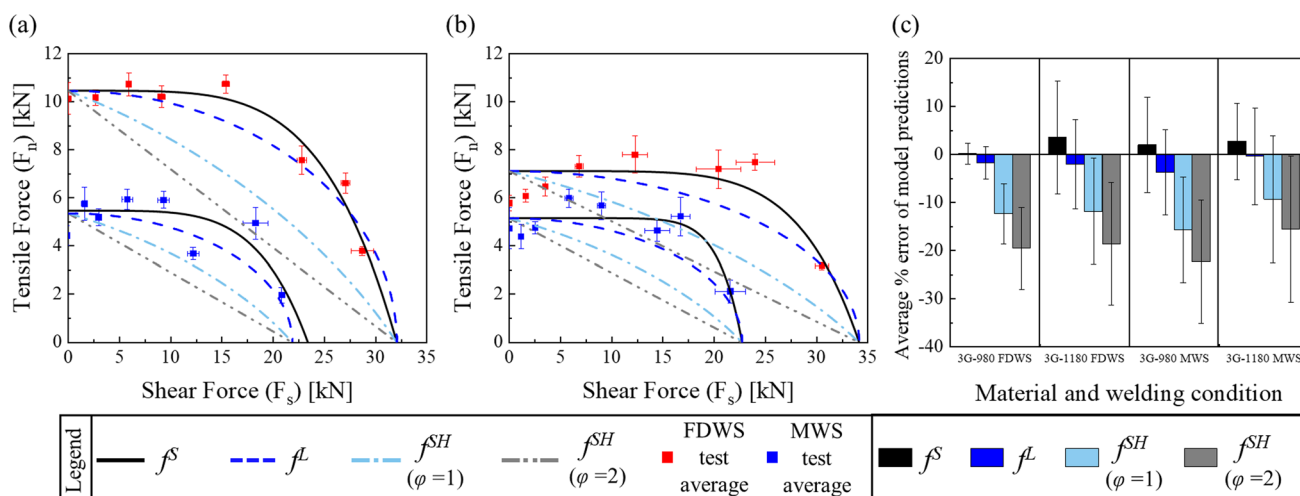


Fig. 17 Comparison between different RSW failure criteria along with the experimental KS-II data points, decomposed according to their final orientations, for (a) 3G-980 and (b) 3G-1180 spot welds

(all shown calibrated models correspond to the final orientation data points upon using the DIC triangular analysis); (c) average error of predictions corresponding to different models calibrated in (a) and (b)

Fig. 18 Three-dimensional RSW failure surfaces calibrated using Eq. 9 and 10 according to the final orientation of the KS-II coupons following the DIC triangular analysis and short arm coach peel tests for (a) 3G-980 FDWS, (b) 3G-1180 FDWS, (c) 3G-980 MWS, and (d) 3G-1180 MWS welding schemes

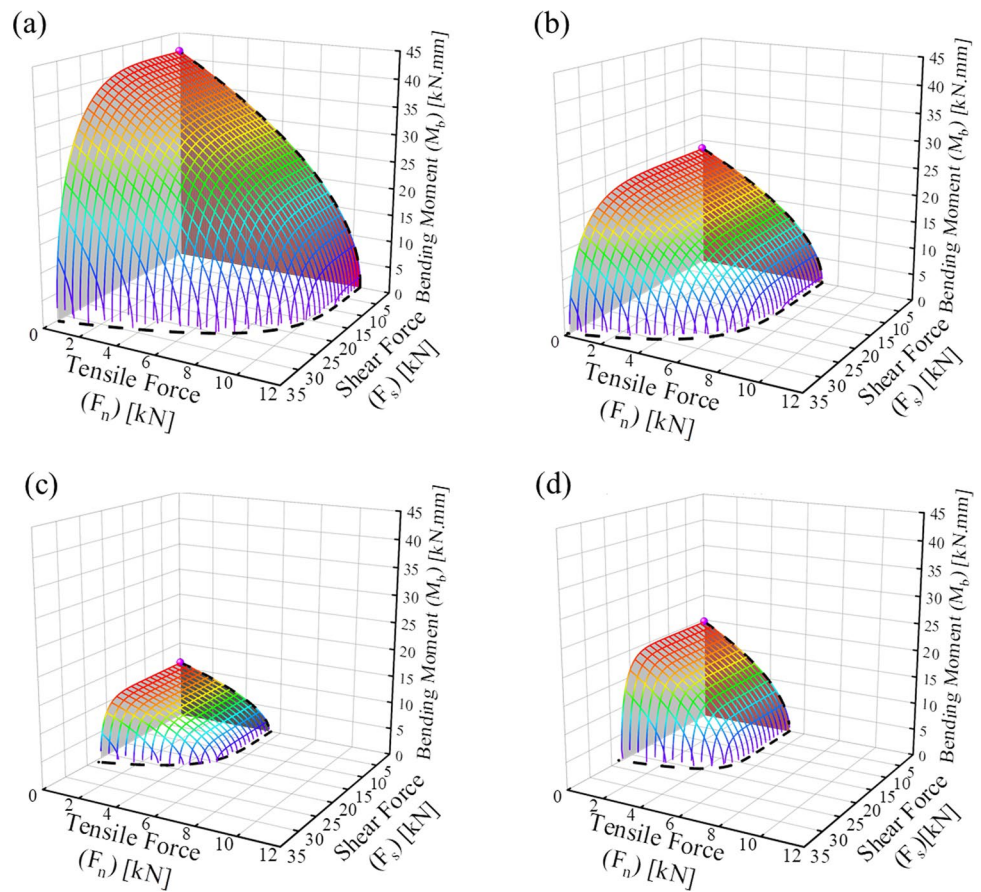


Table 4 Summary of calibrated force-based RSW failure model parameters including failure strengths and exponents

Material and corresponding RSW scheme	Average shear strength (S_s) [kN]	Average tensile strength (S_N) [kN]	Average bending strength (S_B) [kN.mm]	Calibrated exponents		
				a	b	c
3G-980 FDWS	32.071	10.458	41.407	4.67	1.00	2
3G-1180 FDWS	34.160	7.116	23.359	6.00	1.00	2
3G-980 MWS	21.877	5.361	11.021	10.00	1.00	2
3G-1180 MWS	22.743	5.159	19.699	10.00	1.00	2

Calibrated equation $f = \left[\frac{F_s}{S_s}\right]^a + \left[\frac{F_n}{S_N}\right]^b + \left[\frac{M_b}{S_B}\right]^c = 1$

that can be implemented in finite element analysis for a more accurate RSW failure prediction accuracy.

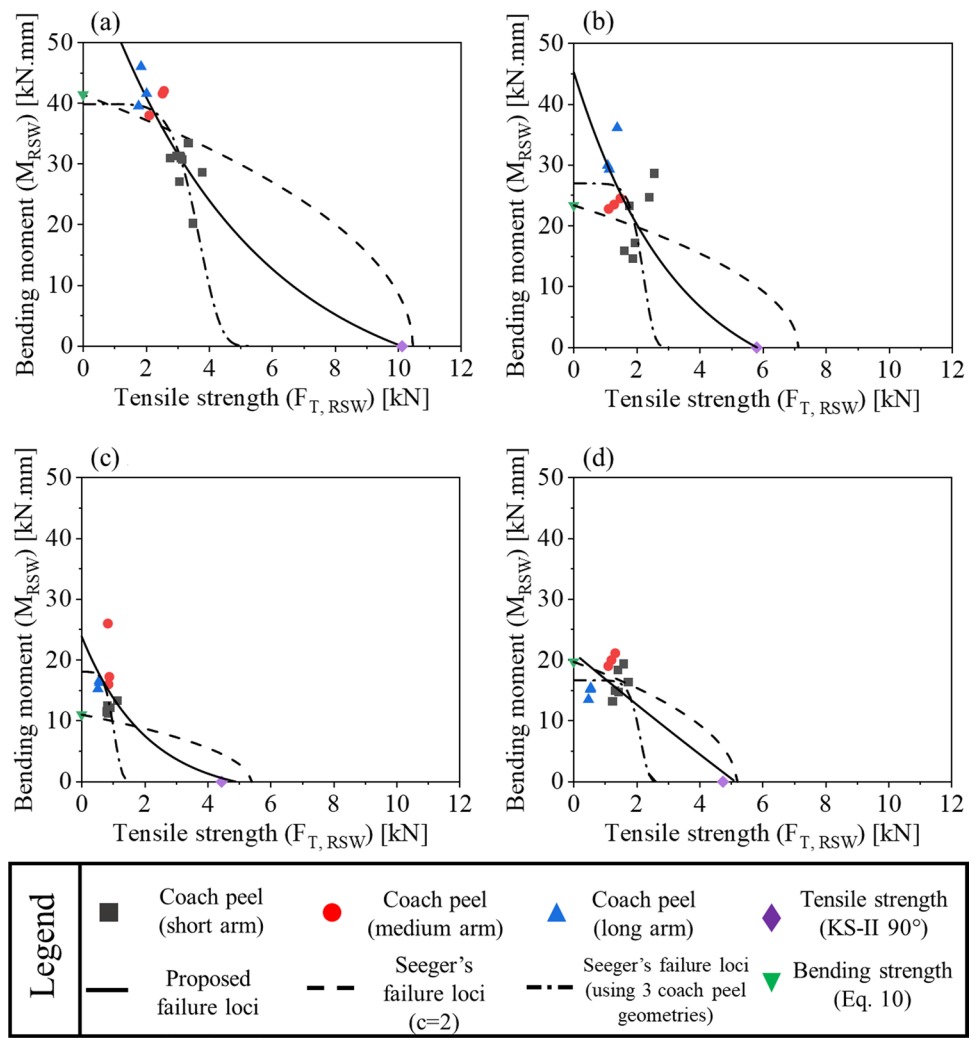
3.5 Evaluating RSW failure models in tensile-bending dominated loading conditions

The critical tensile strengths ($F_{T,RSW}$) and bending moments (M_{RSW}) at the onset of failure are summarized in Fig. 19 for each coach peel test. As shown in Fig. 19, increasing the bending moment arm in FDWS conditions effectively

induced a higher ratio of $\frac{M_{RSW}}{F_{T,RSW}}$. However, due to the IF mode with limited deformation up to the onset of failure, increasing the bending moment arm was not effective in the consistent attainment of a higher $\frac{M_{RSW}}{F_{T,RSW}}$ ratio for MWS welding schemes.

Two different approaches were adopted to calibrate Seeger’s proposed failure loci in tensile-bending conditions shown in Fig. 19. The first approach included the traditional assumption of $c=2$ and S_B calculated from Eq. 10 (as shown earlier in Fig. 18). Calibration using this approach reveals a

Fig. 19 Comparison between failure predictions of proposed and Seeger’s RSW failure loci in tensile-bending dominated conditions for (a) 3G-980 FDWS, (b) 3G-1180 FDWS, (c) 3G-980 MWS, and (d) 3G-1180 MWS conditions. The developed shear strength component is not shown



convex failure locus that poorly predicts the overall trend of critical tensile strengths and bending moments. As an example, at any given average experimental tensile strength of the medium arm coach peel specimens, Seeger’s failure surface of Eq. 9 calibrated using the conventional approach consistently under-predicted failure bending moments by 10.5% for 3G-980 FDWS, 10.3% for 3G-1180 FDWS, 48.8% for 3G-980 MWS, and 14.1% for 3G-1180 MWS. Alternatively, the Seeger model was calibrated using the failure data from

all three coach peel geometries. While using multiple coach peel failure data points increased the overall accuracy of the predictions in combined tension and bending, the tensile strength of the joints was under-predicted by a large margin. Specifically, the tensile strengths were under-predicted by 46.5% for 3G-980 FDWS, 48.3% for 3G-1180 FDWS, 66.2% for 3G-980 MWS, and 45.2% for 3G-1180 MWS conditions. The calibrated failure model parameters using three coach peel geometry failure data are provided in Table 5.

Table 5 Summary of parameters for Seeger’s force-based failure loci in tensile-bending conditions calibrated using failure data from three coach peel geometries

Material and corresponding RSW scheme	Average tensile strength (S_N) [kN]	Average bending strength (S_B) [kN.mm]	Calibrated exponents	
			b	c
3G-980 FDWS	10.123	39.558	6.634	0.0016
3G-1180 FDWS	5.800	26.933	7.767	0.0005
3G-980 MWS	4.440	17.612	5.536	0.0003
3G-1180 MWS	4.741	16.655	9.321	0.0007

An exponential functional form is proposed to better predict the failure of spot welds in tensile-bending loading conditions. The calibrated parameters corresponding to the proposed functional form are outlined in Table 6. The proposed failure loci, compared to the loci proposed by Seeger, predict pure bending strengths that are 57% and 94% higher for 3G-980 FDWS and 3G-1180 FDWS conditions, respectively. The predicted bending strengths are 116% and 4% higher for 3G-980 MWS and 3G-1180 MWS conditions, respectively, in comparison to the bending strengths calculated from Eq. 10. Characterizing the failure of the spot welds at relatively small bending moments (< 10 kN.mm for FDWS and < 5 kN.mm for MWS conditions) required initial bending arms smaller than 7 mm. Attempts for fabrication of such coach peel coupons were unsuccessful due to cracking of the 3G-AHSS at low bending radii and welding limitations associated with the geometry of the utilized RSW C gun.

3.6 Evaluating RSW failure models in tensile-shear loading conditions

The failure loci of the investigated 3G-AHSS in shear-tensile loading conditions are reported for both the “nominal” and “final” orientations. The nominal condition assumes that there is no rotation of the weld, which is valid for tensile-dominated loading but not for shear-dominated orientations. The final condition refers to critical load components determined from the final weld orientation measured using the DIC triangulation method at the peak load frame of the KS-II tests.

The failure loci, shown in Fig. 20, were calibrated using Eq. 7 for both the nominal and final KS-II orientation conditions. The (R^2) values can be seen to reduce when considering the final orientation of the coupons which is associated with the non-linearity in the shear-dominated loading orientations. According to Fig. 20, both investigated materials exhibited relatively similar failure contour profiles in the MWS condition which could be correlated with their similar failure behavior. Most KS-II tests in the MWS condition failed either interfacially, identified via propagation

of a crack through the FZ, or in P-PO mode resulting in a small plug PO area. On the other hand, differences were observed in the FDWS failure contours between the 3G-980 and 3G-1180 spot welds. Specifically, within the tensile-dominated loading orientations the 3G-980 FDWS conditions exhibited between 50 to 65% higher load-bearing capacity on average than the 3G-1180 FDWS spot welds. It was observed that the majority of the tested 3G-980 FDWS joints within the tensile-dominated loading orientations failed in a full nugget PO manner. In contrast, the 3G-1180 FDWS joints typically failed in P-PO mode with a smaller plug area. A representative failure behavior of 3G-980 and 3G-1180 spot welds in the FDWS condition has been shown in Fig. 21. The differences in the local mechanical properties (such as fracture toughness) in regions of crack initiation and propagation between the two steels are thought to be responsible for the observed discrepancy in load-bearing capacity, especially within the tensile-dominated loading orientations.

All calibrated RSW failure models shown in Fig. 20 approach the tensile force (vertical) axis in an orthogonal direction. However, a close examination of the attained final data points reveals expansion of the failure loci in different combined load mixities, specifically within the tensile-dominated region (from 45° to 90° loading orientations). While limited data exists within the literature for the combined loading of spot welds, a similar overall trend of failure data is reported for the combined loading of laser welded high strength low alloy (HSLA) steels [50] and toughened structural adhesives [51]. An empirical and idealized failure model in the form of an exponential function is proposed which can better capture the overall trend of experimental data points and reduce the discrepancies between experimental measurements and model predictions. The calibrated exponential model and its coefficients are shown in Fig. 22(a) and (b), and Table 7, respectively. Alternatively, two independent functional forms can be utilized to reduce the percent errors related to Seeger’s model within the tensile-dominated region. The calibrated loci shown in Fig. 22(c) and (d) use Seeger’s model for capturing the extreme non-linearity within the IF region, whereas a modified version of the power law is calibrated within the PO/P-PO failure regions. The empirical modified power law is as follows:

$$f = \frac{k(m + F_s)^n}{F_n} = 1 \tag{11}$$

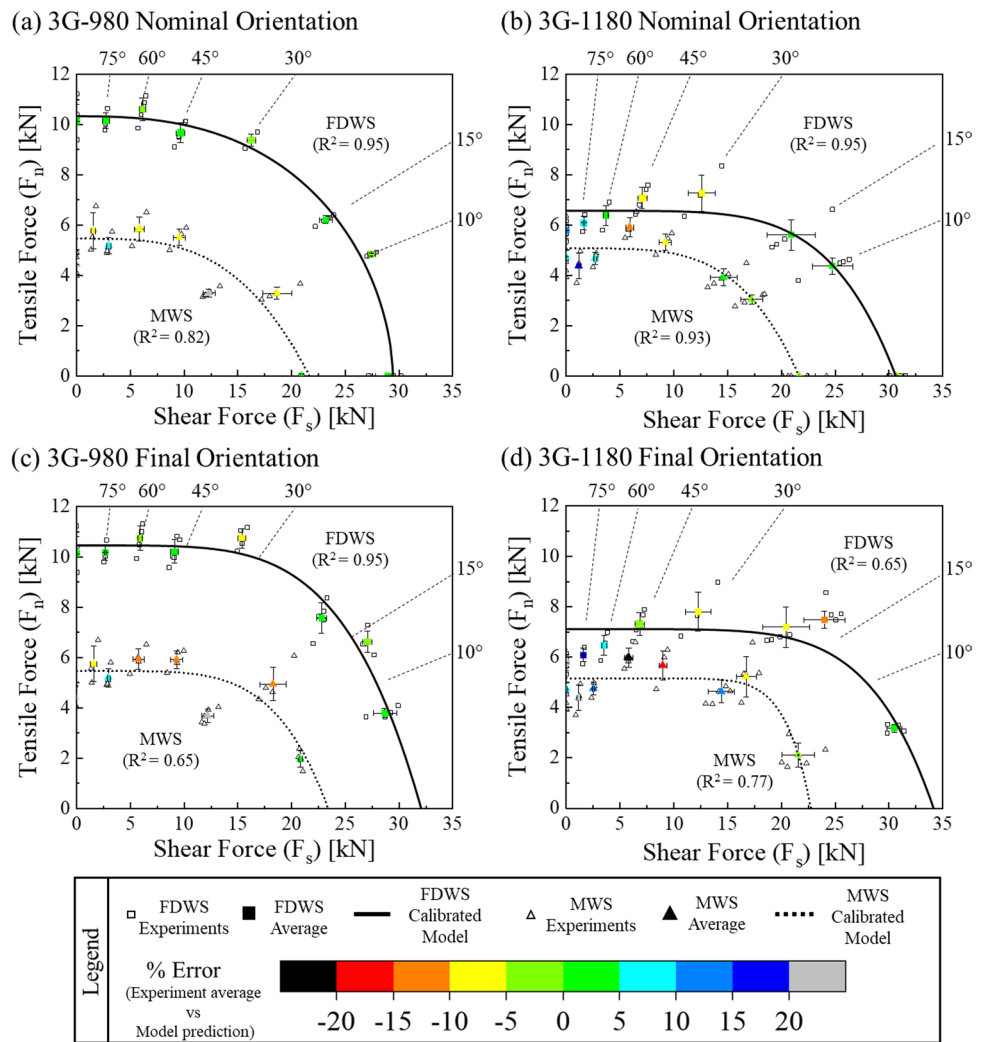
where k , m , and n are the load coefficient, an additive term for vertical axis offset, and load hardening exponent, respectively. The calibrated parameters for these two functions have been summarized in Table 8.

The modified RSW failure loci shown in Figs. 19 and 22, for tensile-bending and tensile-shear loading

Table 6 Summary of calibrated parameters for the proposed force-based RSW failure model in tensile-bending conditions

Material and corresponding RSW scheme	A_1	t_1	M_{b0}
3G-980 FDWS	76.242	4.891	-9.623
3G-1180 FDWS	54.234	3.230	-8.969
3G-980 MWS	26.353	2.073	-2.481
3G-1180 MWS	230.830	53.388	-209.651

Fig. 20 Seeger’s failure loci in shear-tensile loading conditions while considering (a) and (b) the nominal orientation of the 3G-980 and 3G-1180 KS-II coupons; (c) and (d) final orientation of the 3G-980 and 3G-1180 KS-II coupons measured using DIC analysis. The hollow scattered symbols represent the individual data points attained from each test repetition, while the solid symbols show the average values at each loading orientation. The color scale represents the % error of calibrated model predictions compared to the experimental average at each loading orientation



(a) 3G-980 FDWS full nugget pullout

(b) 3G-1180 FDWS partial interfacial partial pullout

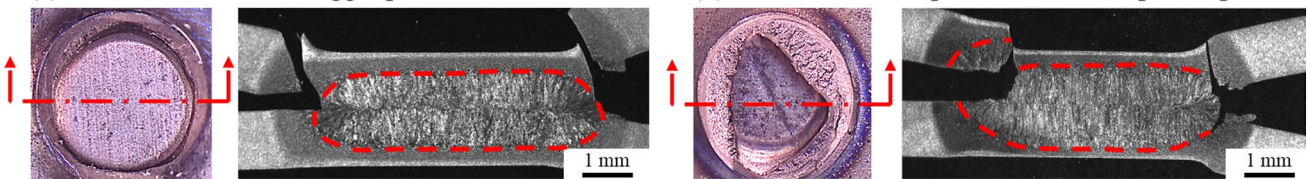


Fig. 21 Representative failure behavior of (a) 3G-980 and (b) 3G-1180 FDWS conditions within the tensile-dominated KS-II loading orientations. The shown micrographs correspond to KS-II tests performed at $\theta=60^\circ$ loading orientation

conditions, respectively, can be input directly into FEA models such as LS-DYNA’s *MAT_100_DA weld material model which is considered a direct enhancement of the *MAT_100 weld material model because it accounts for the failure of spot welds under bending-dominated forces as well as shear and tensile forces. Further characterization of the shear-bending dominated loading cases with different bending arm lengths comparable to the spacing of spot-welded connections in multi-weld components can

lead to additional improvements in current RSW failure prediction procedures.

4 Conclusions

In this study, the force-based RSW failure loci for two grades of 3G-AHSS were developed in shear-tensile and tensile-bending loading conditions. To observe the

Fig. 22 Proposed failure loci in shear-tensile loading conditions while considering the final orientation of the 3G-980 and 3G-1180 KS-II coupons measured using DIC analysis. **a** and **b** show an exponential function with six calibrated coefficients; **(c)** and **(d)** show two different functional forms of failure loci before and after the failure transition points. Seeger’s model was used within the IF region whereas a modified version of the power law equation was used within the PO or P-PO regions. The color scale represents the % error of calibrated model predictions compared to the experimental average at each loading orientation (IF, interfacial failure; PO, pullout failure; P-PO, partial pullout failure)

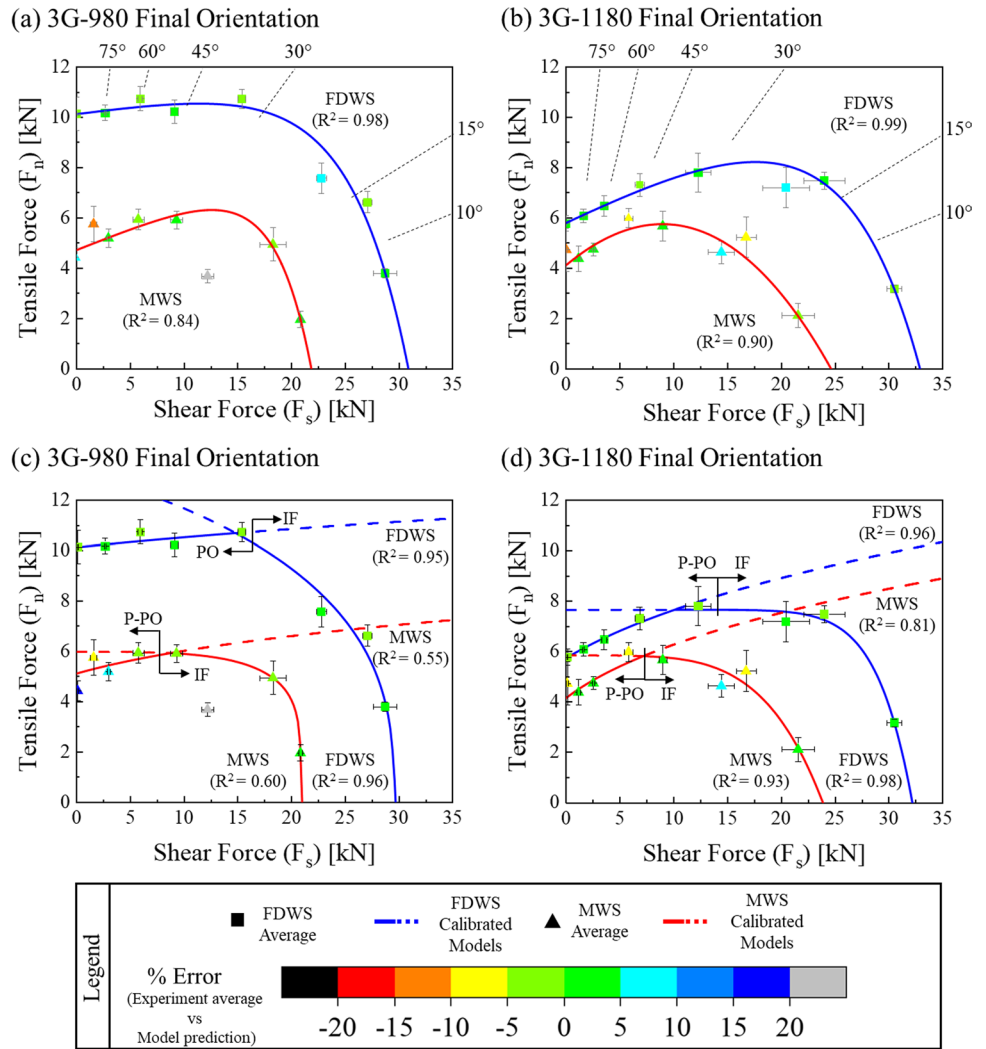


Table 7 Summary of calibrated parameters for an ideal exponential RSW failure model with six coefficients (based on final orientation KS-II data points)

Material and corresponding RSW scheme	Calibrated equation: $f = \frac{F_n}{F_{n0}} - \left[A_1 e^{\frac{F_s - F_{s0}}{t_1}} - A_2 e^{\frac{F_s - F_{s0}}{t_2}} \right] \frac{1}{F_{n0}} = 1$					
	A_1	A_2	F_{s0}	F_{n0}	t_1	t_2
3G-980 FDWS	-0.008	264.71	-9.21	-255.12	5.47	4206.76
3G-1180 FDWS	-1.31E-5	132.23	-68.22	-140.57	7.33	664.59
3G-980 MWS	-2.03E-7	192.48	-40.01	-194.55	3.52	1150.40
3G-1180 MWS	-0.09	2.58	-946.87	-607.21	99.69	143.62

Table 8 Summary of calibrated parameters for two RSW failure models valid before and after failure transitions (based on final orientation KS-II data points)

Material and corresponding RSW scheme	$f = \frac{k(m+F_s)^n}{F_n} = 1$			$f = \left[\frac{F_s}{S_s} \right]^a + \left[\frac{F_n}{S_n} \right]^b = 1$			
	k	m	n	S_s	S_n	a	b
3G-980 FDWS	5.60	37.61	0.16	30.10	14	1.29	2.62
3G-1180 FDWS	2.88	7.54	0.34	32.18	7.66	10	1
3G-980 MWS	3.09	9.40	0.22	20.85	5.98	3.65	5.05
3G-1180 MWS	2.49	4.37	0.34	23.88	5.84	4.58	1

influence of nugget diameter on the size and general shape of the failure loci, different RSW process parameters were selected to produce different nugget sizes, referred to as FDWS and MWS, with high and low heat inputs, respectively. The following conclusions are drawn:

- Comparison between several existing force-based RSW failure criteria revealed that the equation suggested by Seeger et al. [29] has the highest flexibility in capturing the experimental trends specifically in shear-tension loading conditions characterized by KS-II tests with an average over-prediction error between 0.2% and 3.5% for various loading orientations. The criterion proposed by Song and Huh [31] was found the most conservative in the prediction of 3G-AHSS RSW failure in the same loading condition with between 9.2% and 22.3% under-predictions for various shear-tension loading conditions.
- Experimental shear and tensile failure load components of the KS-II tests revealed expansion of the failure locus as the shear component of applied force increased within the tensile-dominated loading orientations. Changes in the dominant failure mechanism of spot welds from PO/P-PO to IF were found responsible for such trends. None of the existing force-based RSW failure criteria were found capable of predicting such experimental behaviors. Suitable alternative functional forms were proposed to accurately capture the expansion/contraction of the failure loci in tensile-dominated loading orientations.
- Assessing the validity of predictions by Seeger's failure loci in tension-bending conditions necessitated performing coach peel tests with different initial bending moment arm lengths. Novel DIC-based methodologies were developed to account for the severe deformation of the coupons and the reduction of the effective bending arm. Bending moments and load components throughout the tests were plotted against local projected nugget orientation and displacements, respectively, which allowed for the precise calculation of critical moments and load components applied to the projected RSW at the onset of failure.
- Results indicated that doubling the initial bending arm of the coach peel coupons from short arm to long arm geometry reduces the critical tensile forces ($F_{T, RSW}$) applied to the spot weld between 38.3% and 64.3% whereas the effective bending moment (M_{RSW}) at the onset of failure increases between 32.1% and 53.5% for the weld conditions considered. The FDWS conditions exhibited consistent total energy absorption capabilities ($E_{Total, RSW}$) as the bending arm increased. While the $E_{Total, RSW}$ remained virtually unchanged as the coach peel geometry changed in FDWS cases, the ratio of $E_{T, RSW}/E_{Total, RSW}$ decreased

by 34.1% and 17.5% for 3G-980 and 3G-1180 FDWS conditions. Meanwhile, the $E_{M, RSW}/E_{Total, RSW}$ ratio increased by 34.1% and 34.7% upon changing the coach peel geometry from short arm to long arm for 3G-980 and 3G-1180 FDWS conditions, respectively.

- Coach peel test results revealed an exponentially decreasing failure loci between the bending moment and normal force in contrast to the assumed convex relationship of Seeger's model. The Seeger RSW failure loci over-predicted the critical M_{RSW} of the short-arm geometry up to 66.1%. An exponential functional form was proposed and calibrated that successfully addresses the deficiencies in the prediction accuracy of spot weld failure in tension-bending loading cases.

Authors contributions All authors contributed to the study conception and design. Material preparation, data collection and analysis were performed by Mohammad Shojaee, Cameron Tolton, and Abdelbaset Midawi. The first draft of the manuscript was written by Mohammad Shojaee and all authors commented on previous versions of the manuscript. All authors read and approved the final manuscript.

Funding The authors would like to thank the Auto/Steel Partnership (A/SP) team members and the Natural Sciences and Engineering Research Council (NSERC) of Canada for providing the parent sheet metals and financial support to carry out this work.

Declarations

Competing interests The authors have no relevant financial or non-financial interests to disclose.

References

1. Zielinski J, Andreucci R, Rajagopalan N, Aktas CB (2018) Prospects for meeting the corporate average fuel economy standards in the U.S. *Resour Conserv Recycl* 136:466–72. <https://doi.org/10.1016/j.resconrec.2018.03.026>
2. Keith DR, Houston S, Naumov S (2019) Vehicle fleet turnover and the future of fuel economy. *Environ Res Lett* 14. <https://doi.org/10.1088/1748-9326/aaf4d2>
3. Zhao J, Jiang Z (2018) Thermomechanical processing of advanced high strength steels. *Prog Mater Sci* 94:174–242. <https://doi.org/10.1016/j.pmatsci.2018.01.006>
4. Kalashami AG, Digiiovanni C, Razmpoosh MH, Goodwin F, Zhou NY (2020) The effect of silicon content on liquid-metal-embrittlement susceptibility in resistance spot welding of galvanized dual-phase steel. <https://doi.org/10.1016/j.jmapro.2020.07.008>
5. Zhang S, Ghatei-Kalashami A, Midawi ARH, Zhou NY (2022) A Comparison between Hardness-Scaling and Ball-Indentation Techniques on Predicting Stress/Strain Distribution and Failure Behavior of Resistance Spot Welded Advanced High Strength Steel. *J Manuf Sci Eng Trans ASME* 144. <https://doi.org/10.1115/1.4053730/1134922>

6. Figueredo B, Ramachandran DC, Macwan A, Biro E (2021) Failure behavior and mechanical properties in the resistance spot welding of quenched and partitioned (Q&P) steels. *Weld World* 65:2359–2369. <https://doi.org/10.1007/s40194-021-01179-z>
7. Pouranvari M, Marashi SPH (2013) Critical review of automotive steels spot welding: Process, structure and properties. *Sci Technol Weld Join* 18:361–403. <https://doi.org/10.1179/1362171813Y.0000000120>
8. Mohamadizadeh A, Biro E, Worswick M. novel double-half spot weld testing technique for damage progress and failure analysis using digital image correlation techniques 123AD. <https://doi.org/10.1007/s11340-021-00743-4>
9. Mohamadizadeh A, Biro E, Worswick M (2022) Failure characterization and meso-scale damage modeling of spot welds in hot-stamped automotive steels using a hardness-mapping approach. *Eng Fract Mech* 268:108506. <https://doi.org/10.1016/j.engfractmech.2022.108506>
10. Ma Y, Takikawa A, Nakanishi J, Doira K, Shimizu T, Lu Y et al (2021) Measurement of local material properties and failure analysis of resistance spot welds of advanced high-strength steel sheets. *Mater Des* 201. <https://doi.org/10.1016/J.MATDES.2021.109505>
11. Ghassemi-Armaki H, Khan Q, Gill AS, Zilincik S (2017) Characterization and modeling of spot-weld joints in press hardening steels associated with softening in heat affected zone. 11th Eur LS-DYNA Conf 1–13
12. Wung P (2001) A force-based failure criterion for spot weld design. *Exp Mech* 41(1):107–13. <https://doi.org/10.1007/BF02323112>
13. Lin S-H, Pan J, Wu S, Tyan T (2004) Failure loads of spot weld specimens under impact opening and shear loading conditions. *Exp Mech* 44(2):147–57. <https://doi.org/10.1007/BF02428174>
14. Chabok A, Cao H, van der Aa E, Pei Y (2022) New insights into the fracture behavior of advanced high strength steel resistance spot welds. *J Mater Process Technol* 301:117433. <https://doi.org/10.1016/J.JMATPROTEC.2021.117433>
15. Mohamadizadeh A, Biro E, Worswick M (2020) Shear band formation at the fusion boundary and failure behaviour of resistance spot welds in ultra-high-strength hot-stamped steel. *Sci Technol Weld Join* 25:556–563. <https://doi.org/10.1080/13621718.2020.1773057>
16. Sherepenko O, Mohamadizadeh A, Zvorykina A, Worswick M, Biro E, Jüttner S (2021) Determination of resistance spot weld failure path in ultra-high-strength press-hardened steel by control of fusion boundary transient softening. *J Mater Sci* 56:14287–14297. <https://doi.org/10.1007/S10853-021-06165-W/FIGURES/10>
17. Midawi ARH, Shojaee M, Mohamadizadeh A, Bourque C, Ghassemi-Aramki H, Worswick M et al (2022) A novel technique to measure the local mechanical properties of third generation advanced high strength steel resistance spot welds. *Forces Mech* 9. <https://doi.org/10.1016/j.finmec.2022.100150>
18. Shamsujjoha M, Enloe CM, Chuang AC, Coryell JJ, Ghassemi-Armaki H (2021) Mechanisms of paint bake response in resistance spot-welded first and third generation AHSS. *Materialia* 15:100975. <https://doi.org/10.1016/j.mtla.2020.100975>
19. Ma Y, Yu Y, Geng P, Ihara R, Maeda K, Suzuki R et al (2021) Fracture modeling of resistance spot welded ultra-high-strength steel considering the effect of liquid metal embrittlement crack. *Mater Des* 210. <https://doi.org/10.1016/J.MATDES.2021.110075>
20. Ghassemi-Armaki H, Biro E, Sadagopan S (2017) Advanced characterization of HAZ softening of AHSS for crash modeling. *ISIJ Int* 57:1451–1460. <https://doi.org/10.2355/isijinternational.ISIJNT-2016-649>
21. Samadian P, ten Kortenaar L, Omer K, Butcher C, Worswick MJ (2020) Fracture characterization of tailored Usibor® 1500-AS and damage modelling based on a coupled-micromechanical-phenomenological strategy. *Eng Fract Mech* 223:106785. <https://doi.org/10.1016/J.ENGFRACMECH.2019.106785>
22. Tamizi M, Pouranvari M, Movahedi M (2017) Welding metallurgy of martensitic advanced high strength steels during resistance spot welding. *Sci Technol Weld Join* 22:327–335. <https://doi.org/10.1080/13621718.2016.1240979>
23. Wang W, Zhu Q, Liu C, Wei X (2019) An investigation on the resultant-based failure criterion for resistance spot welding joint in crush test. *Int J Crashworthiness* 24:152–162. <https://doi.org/10.1080/13588265.2017.1421012>
24. Livermore Software Technology Corporation (2015) LS-DYNA Keyword User's Manual - Volume II. r:6581
25. Pouranvari M, Marashi SPH (2012) Failure of resistance spot welds: Tensile shear versus coach peel loading conditions. *Ironmak Steelmak* 39:104–111. <https://doi.org/10.1179/1743281211Y.0000000066>
26. Hu S, Haselhuhn AS, Ma Y, Li Y, Carlson BE, Lin Z (2021) Influencing mechanism of inherent aluminum oxide film on coach peel performance of baked Al-Steel RSW. *Mater Des* 197:109250. <https://doi.org/10.1016/j.matdes.2020.109250>
27. Xu Z, Tian C, Mao L, Tian H, Yi B, Ling H (2023) A mechanical properties and failure mechanism study for resistance spot welded AHSSs under coach-peel and lap-shear loads. *Eng Fract Mech* 290:109474. <https://doi.org/10.1016/j.engfractmech.2023.109474>
28. Lin SH, Pan J, Tyan T, Prasad P (2003) A general failure criterion for spot welds under combined loading conditions. *Int J Solids Struct* 40:5539–5564. [https://doi.org/10.1016/S0020-7683\(03\)00341-X](https://doi.org/10.1016/S0020-7683(03)00341-X)
29. Seeger F, Feucht M, Frank T, Keding B, Haufe A (2005) An investigation on spot weld modelling for crash simulation with LS-DYNA. 4th LS-DYNA Conf, Bamberg, Germany 1–12
30. Tolton CJ (2020) Characterization of spot weld failure within weld groups under predominantly shear loading. Master's thesis. University of Waterloo
31. Song JH, Huh H (2011) Failure characterization of spot welds under combined axial–shear loading conditions. *Int J Mech Sci* 53:513–525. <https://doi.org/10.1016/J.IJMECSCI.2011.04.008>
32. Langrand B, Combescure A (2004) Non-linear and failure behaviour of spotwelds: a “global” finite element and experiments in pure and mixed modes I/II. *Int J Solids Struct* 41:6631–6646. <https://doi.org/10.1016/J.IJSOLSTR.2004.06.009>
33. Lin SH, Pan J, Wu SR, Tyan T, Wung P (2001) Failure loads of spot welds under combined opening and shear static loading conditions. *Int J Solids Struct* 39:19–39. [https://doi.org/10.1016/S0020-7683\(01\)00187-1](https://doi.org/10.1016/S0020-7683(01)00187-1)
34. Pandya KS, Grolleau V, Roth CC, Mohr D (2020) Fracture response of resistance spot welded dual phase steel sheets: Experiments and modeling. *Int J Mech Sci* 187:105869. <https://doi.org/10.1016/j.ijmecsci.2020.105869>
35. Shojaee M, Tolton C, Midawi ARH, Butcher C, Ghassemi-armaki H, Worswick M (2022) Influence of loading orientation on mechanical properties of spot welds. *Int J Mech Sci* 224:107327. <https://doi.org/10.1016/j.ijmecsci.2022.107327>
36. Yurioka N, Suzuki H, Ohshita S, Saito S (1983) Determination of necessary preheating temperature in steel welding. *Weld J* 62:147–153
37. American Welding Society (2012) AWS D8.9M, 3rd edn. - Test method for evaluating the resistance spot welding behavior of automotive sheet steel materials
38. American Welding Society (2021) AWS D8.1M, 3rd edn. - Specification for automotive weld quality resistance spot welding of steel
39. Song S, Shojaee M, Midawi ARH, Sherepenko O, Ghassemi-Armaki H, Biro E (2023) Influence of expulsion and heat extraction resulting from changes to electrode force on liquid metal embrittlement during resistance spot welding. *J Mater Res Technol* 23:1458–1470. <https://doi.org/10.1016/J.JMRT.2023.01.093>

40. Khameneh F, Abedini A, Butcher C (2021) Lengthscale effects in optical strain measurement for fracture characterization in simple shear. *Int J Fract* 232:153–180. <https://doi.org/10.1007/s10704-021-00598-9>
41. Anderson D, Butcher C, Pathak N, Worswick MJ (2017) Failure parameter identification and validation for a dual-phase 780 steel sheet. *Int J Solids Struct* 124:89–107. <https://doi.org/10.1016/j.ijsolstr.2017.06.018>
42. Shojaee M, Midawi ARH, Barber B, Ghassemi-Armaki H, Worswick M, Biro E (2021) Mechanical properties and failure behavior of resistance spot welded third-generation advanced high strength steels. *J Manuf Process* 65:364–372. <https://doi.org/10.1016/j.jmapro.2021.03.047>
43. Pawar S, Singh AK, Park K-S, Choi S-H (2023) Effect of welding current on the microstructural evolution and lap-shear performance of resistance spot-welded 340BH steel. <https://doi.org/10.1016/j.matchar.2023.113126>
44. Langrand B, Markiewicz E (2010) Strain-rate dependence in spot welds: Non-linear behaviour and failure in pure and combined modes I/II. *Int J Impact Eng* 37:792–805. <https://doi.org/10.1016/j.ijimpeng.2010.01.004>
45. Chao YJ (2003) Ultimate strength and failure mechanism of resistance spot weld subjected to tensile, shear, or combined tensile/shear loads. *J Eng Mater Technol Trans ASME* 125:125–132. <https://doi.org/10.1115/1.1555648>
46. Betiku OT, Shojaee M, Sherepenko O, Midawi ARH, Chertov AM, Ghassemi-Armaki H et al (2022) Optimizing post-weld performance of press-hardened steel resistance spot welds by controlling fusion zone porosity. *Weld World* 66:1733–1746. <https://doi.org/10.1007/s40194-022-01332-2>
47. Lee Y, Wehner TJ, Lu M, Morrisett T, Pakalnins E (1998) Ultimate strength of resistance spot welds subjected to combined tension and shear. *J Test Eval* 26:213–9
48. Seeger F, Michel G, Blanquet M (2008) Investigation of spot weld behavior using detailed modeling technique. 7th LS-DYNA Conf, Bamberg, Germany 29–38
49. Lim J, Ha J, Oh C (2015) Practical Failure Criterion of Spot Weld for Crash Simulation. 10th Eur LS-DYNA Conf, Wurzburg, Germany 1–7
50. Ha J, Huh H (2013) Failure characterization of laser welds under combined loading conditions. *Int J Mech Sci* 69:40–58. <https://doi.org/10.1016/j.ijmecsci.2013.01.022>
51. Watson B, Worswick MJ, Cronin DS (2020) Quantification of mixed mode loading and bond line thickness on adhesive joint strength using novel test specimen geometry. *Int J Adhes Adhes* 102:102682. <https://doi.org/10.1016/j.ijadhadh.2020.102682>

Publisher's Note Springer Nature remains neutral with regard to jurisdictional claims in published maps and institutional affiliations.

Springer Nature or its licensor (e.g. a society or other partner) holds exclusive rights to this article under a publishing agreement with the author(s) or other rightsholder(s); author self-archiving of the accepted manuscript version of this article is solely governed by the terms of such publishing agreement and applicable law.